The Astrophysical Journal, 807:173 (17pp), 2015 July 10 doi:10.1088/0004-637X/807/2/173

AN ELEMENTAL ASSAY OF VERY, EXTREMELY, AND ULTRA-METAL-POOR STARS*

T. Hansen[1], C. J. Hansen[2], N. Christlieb[1], T. C. Beers[3], D. Yong[4], M. S. Bessell[4], A. Frebel[5], A. E. García Pérez[6], V. M. Placco[3], J. E. Norris[4], and M. Asplund[4]

[1] Landessternwarte, ZAH, Königstuhl 12, D-69117 Heidelberg, Germany; thansen@lsw.uni-heidelberg.de

[2] Dark Cosmology Centre, Niels Bohr Institute, University of Copenhagen, Juliane Maries Vej 30, DK-2100 Copenhagen Ø, Denmark

[3] Department of Physics and JINA-CEE: Joint Institute for Nuclear Astrophysics—Center for the Evolution of the Elements, University of Notre Dame, Notre Dame, IN 46556, USA

[4] Research School of Astronomy and Astrophysics, The Australian National Univeristy, Weston, ACT 2611, Australia

[5] Kavli Institute for Astrophysics and Space Research and Department of Physics, Massachusetts Institute of Technology, Cambridge, MA 02139, USA

[6] Instituto de Astrofísica de Canarias, E38205 La Laguna, Tenerife, Spain and Departamento de Astrofísica, Universidad de La Laguna, E-38206 La Laguna, Tenerife, Spain

Received 2015 March 23; accepted 2015 June 1; published 2015 July 9

ABSTRACT

We present a high-resolution elemental-abundance analysis for a sample of 23 very metal-poor ([Fe/H] < −2.0) stars, 12 of which are extremely metal-poor ([Fe/H] < −3.0), and 4 of which are ultra-metal-poor ([Fe/H] < −4.0). These stars were targeted to explore differences in the abundance ratios for elements that constrain the possible astrophysical sites of element production, including Li, C, N, O, the α-elements, the iron-peak elements, and a number of neutron-capture elements. This sample substantially increases the number of known carbon-enhanced metal-poor (CEMP) and nitrogen-enhanced metal-poor (NEMP) stars—our program stars include eight that are considered "normal" metal-poor stars, six CEMP-*no* stars, five CEMP-*s* stars, two CEMP-*r* stars, and two CEMP-*r*/*s* stars. One of the CEMP-*r* stars and one of the CEMP-*r*/*s* stars are possible NEMP stars. We detect lithium for three of the six CEMP-*no* stars, all of which are Li depleted with respect to the Spite plateau. The majority of the CEMP stars have [C/N] > 0. The stars with [C/N] < 0 suggest a larger degree of mixing; the few CEMP-*no* stars that exhibit this signature are only found at [Fe/H] < −3.4, a metallicity below which we also find the CEMP-*no* stars with large enhancements in Na, Mg, and Al. We confirm the existence of two plateaus in the absolute carbon abundances of CEMP stars, as suggested by Spite et al. We also present evidence for a "floor" in the absolute Ba abundances of CEMP-*no* stars at A(Ba) ∼ −2.0.

Key words: Galaxy: formation – Galaxy: halo – Galaxy: stellar content – nuclear reactions, nucleosynthesis, abundances – stars: abundances

1. INTRODUCTION

In recent years, high-resolution spectroscopic analyses of samples of stars with metallicities significantly below solar have grown to the point that one can begin to establish the general behaviors of elemental abundance ratios associated with production by the first few generations of stars to form the Galaxy (for a recent review see, e.g., Frebel & Norris 2015). These "statistical" samples are particularly valuable when the data are analyzed in a self-consistent manner (e.g., Yong et al. 2013), so that comparisons of derived abundance ratios are not plagued by the scatter introduced from the different assumptions and procedures used by individual researchers, which can be sufficiently large as to obscure important details.

Of particular interest to this effort is the class of stars that, despite their overall low abundances of iron-peak elements, exhibit large overabundances of C (as well as N and O) in their atmospheres, the so-called carbon-enhanced metal-poor (CEMP) stars (Beers et al. 1992; Beers & Christlieb 2005; Norris et al. 2013b). This class comprises a number of subclasses (originally defined by Beers & Christlieb 2005), based on the behavior of their neutron-capture elements: (1) CEMP-*no* stars, which exhibit no overabundances of *n*-capture elements; (2) CEMP-*s* stars, which show *n*-capture overabundances consistent with the slow neutron-capture process; (3) CEMP-*r* stars, with *n*-capture overabundances associated with the rapid neutron-capture process; and (4) CEMP-*r*/*s* stars, which exhibit *n*-capture overabundances that suggest contribution from both the slow and rapid neutron-capture processes. Each of these subclasses appears to be associated with different element-production histories; thus, their study provides insight into the variety of astrophysical sites in the early Galaxy that were primarily responsible for their origin. The CEMP-*no* stars are of special importance, as the preponderance of evidence points to their being associated with elemental-abundance patterns that were produced by the very first generation of massive stars (Norris et al. 2013b; Hansen et al. 2014; Maeder et al. 2014); thus, they potentially provide a unique probe of the first mass function in the early universe along with providing information on the nucleosynthesis and properties of the first stars.

In a previous paper, Hansen et al. (2014, hereafter Paper I) provided a detailed study of the elemental abundances for a sample of four ultra-metal-poor (UMP) stars with [Fe/H] < −4.0, three of which are clear examples of CEMP-*no* stars. Here we supplement this sample with an additional 19 stars, exploring a wider range of metallicity. This allows for the inclusion of additional examples of CEMP-*no*, CEMP-*s*, CEMP-*r*, and CEMP-*r*/*s* stars (two of which qualify as possible nitrogen-enhanced metal-poor [NEMP] stars), providing a more complete picture of the variety of elemental-abundance patterns for stars of very low metallicity.

This paper is outlined as follows. Section 2 summarizes our observations and data analysis techniques. Section 3 presents

* Based on observations made with the European Southern Observatory telescopes.

our abundance analysis results, and Section 4 provides a summary and brief discussion of their implications.

2. OBSERVATIONS AND DATA ANALYSIS

Our sample of 23 very metal-poor (VMP; [Fe/H] $\leqslant -2.0$), extremely metal-poor (EMP; [Fe/H] $\leqslant -3.0$), and UMP ([Fe/H] $\leqslant -4.0$) stars presented here was originally selected from the Hamburg/ESO Survey (HES; Frebel et al. 2006; Christlieb et al. 2008), followed up with medium-resolution spectroscopy on a variety of 2–4 m class telescopes (AAT 3.9 m, CTIO 4 m, CTIO 1.5 m, ESO 3.6 m, KPNO 4 m, SOAR 4 m, SSO 2.3 m, and UKST 1.2 m), and then observed at high spectral resolution with VLT/UVES (Dekker et al. 2000). Paper I describes the observations and analysis of the four UMP stars in this sample.

The high-resolution spectroscopy of the stars in our sample was performed with UVES using the dichroic (DIC) beam splitter, allowing simultaneous observation with the blue and red arm, in order to cover a spectral range including a large number of chemical elements. Three different settings were used: DIC (blue central wavelength + red central wavelength), covering the following wavelengths—DIC1 (390+580) blue: 3260–4450 Å, red: 4760–6840 Å, DIC2 (346+760) blue: 3030–3880 Å, red: 5650–9460 Å, and DIC2 (437+760) blue: 3730–4990 Å, red: 5650–9460 Å. The spectral resolving power varies with the choice of wavelength setting and slit width. The average resolving power of the spectra is $R \sim 45{,}000$. Positions, observation dates, exposure times, and specific settings for the individual stars in the sample are listed in Table 1.

The spectra were reduced using the UVES reduction pipeline version 4.9.8. Radial-velocity shifts of the spectra were obtained using the IRAF[7] task FXCOR. Individual spectra were cross-correlated with a template spectrum obtained during the same observation run. For the 2005 run, HE 0134–1519 and HD 2796 were used as templates, for which we find $V_r = 244.0\,\mathrm{km\,s^{-1}}$ and $V_r = -14.7\,\mathrm{km\,s^{-1}}$, respectively. For the 2006 run, HD 140283 was used, for which we find $V_r = -185.4\,\mathrm{km\,s^{-1}}$. For stars with multiple observations, the individual spectra were co-added with the IRAF SCOMBINE task. Finally, the radial-velocity-shifted (and combined) spectrum was normalized. Table 2 lists the derived radial velocities and signal-to-noise ratios (S/Ns) at specific wavelengths for the different spectra. When a wavelength region is covered by more than one setting, the one having the highest S/N is listed. Note that, because the spectra were only obtained spanning at most a few nights, these data are not suitable for evaluation of the binary nature of our stars. However, the high accuracy of our derived radial velocities (typically better than $1\,\mathrm{km\,s^{-1}}$) should prove useful for comparison with future binarity studies.

Three of the stars in our sample are rediscoveries and have radial velocities reported in the literature. These three stars are HE 0054–2542 (CS 22942–019, CD-26:304), HE 0411–3558 (CS 22186–005), and HE 0945–1435. Preston & Sneden (2001) found HE 0054–2542 to be in a binary system with a period of 2800 days, while Norris et al. (1996) report $V_r = 192.4\,\mathrm{km\,s^{-1}}$ for HE 0411–3558, close to our value of $V_r = 196.2\,\mathrm{km\,s^{-1}}$, and Norris et al. (2013a) report $V_r = 121.8.4\,\mathrm{km\,s^{-1}}$ for HE 0945–1435, where we find $V_r = 144.8\,\mathrm{km\,s^{-1}}$, suggesting that it is a likely binary star.

[7] IRAF is distributed by the National Astronomy Observatory, Inc., under cooperative agreement with the National Science Foundation.

2.1. Stellar Parameters

The stellar atmospheric parameters were determined following most of the steps outlined in Yong et al. (2013) and in Paper I, so that the results of the abundance analyses of their sample and ours can be usefully combined.

The effective temperature ($T_{\rm eff}$) was, for the majority of the stars, determined by fitting spectrophotometric observations of the star with model-atmosphere fluxes (Bessell 2007; Norris et al. 2013a). For this step, medium-resolution spectra were obtained with the Wide Field Spectrograph (Dopita et al. 2007) on the Australian National University 2.3 m telescope at Siding Spring Observatory during 2012. This is a double-beam spectrograph using a dichroic mirror to separate the blue and red regions. The spectrograph covers the wavelength ranges 3000–6200 Å and 6000–9700 Å in the blue and red, respectively, with a resolution of 2 Å. The observations, data reduction, and analysis were performed as described in Section 4.1 of Norris et al. (2013a). The reduced spectra were cross-correlated against a grid of MARCS atmosphere models (Gustafsson et al. 2008) using the PHYTON program fitter, written by S. J. Murphy. The MARCS models have parameters ranging in $T_{\rm eff}$ from 2500 to 8000 K, in steps of 100 K from 2500 to 4000 K, and in steps of 250 K from 4000 to 8000 K. Surface gravity ($\log g$) values for the grid were between −1.0 (cgs) and 5.5 (cgs) in steps of 0.5 dex, and metallicities between −5.0 and +1.0 in variable steps. As the stars in this sample all have very low metallicities, α-enhanced models were used, with $[\alpha/\mathrm{Fe}] = +0.25$ for $-1.5 \leqslant [\mathrm{Fe/H}] \leqslant -0.5$ and $[\alpha/\mathrm{Fe}] = +0.4$ for $-5.0 \leqslant [\mathrm{Fe/H}] < -1.5$.

For two stars in the sample (marked in Table 3) we did not have spectrophotometric observations. The effective temperatures for these stars were determined from broadband photometry, using the $V-K$ color index, as this is least affected by metallicity (Alonso et al. 1999). The V and K magnitudes for the stars are listed in Table 3. The Two Micron All Sky Survey (2MASS) K magnitudes were converted to the Johnson photometric system using the filter conversion $K_{\rm Johnson} = K_{\rm 2MASS} + 0.044$ (Bessell 2005). Reddening values, $E(B-V)$, are adopted from Schlegel et al. (1998); values exceeding 0.1 mag were corrected according to Bonifacio et al. (2000). These values were then converted to $E(V-K)$, using the relation from Alonso et al. (1996), $E(V-K) = 2.72\,E(B-V)$. The final de-reddened $V-K$ colors were thus found from the following equation: $V - K_{0,\rm Johnson} = V_{\rm Johnson} - K_{\rm 2MASS} + 0.044 - 2.72\,E(B-V)$.

To estimate the effective temperatures, we used the calibration of Alonso et al. (1996), as this provides temperatures that are in good agreement with the scale used for the majority of our sample. We determined temperatures using this method for as many stars in the sample as possible, in order to estimate the offset between the two temperature scales. We found an average offset of +30 K between the two temperature scales and have corrected the temperatures determined from the $V-K$ colors accordingly ($T_{\rm eff} = T_{{\rm eff},V-K} + 30$). The V and $B-V$ photometry listed for HE 0010–3422 in Table 3 is almost certainly in error, as it results in a temperature ∼1500 K below what was found from the spectrophotometric observations. Owing to this large difference, this star has been

Table 1
Observation Log

Stellar ID	R.A.	Decl.	Date	Exp. (s)	Slit (arcsec)[a]	Setting[b]
HE 0010–3422	00 13 08.9	−34 05 55	2005 Nov 18	3600	1.2/1.2	390/580
HE 0054–2542[c,e]	00 57 18.0	−25 26 09	2005 Nov 19	1200	1.0/1.0	390/580
HE 0100–1622	01 02 58.5	−16 06 31	2005 Nov 18	3600	1.2/1.2	390/580
HE 0109–4510	01 12 08.1	−44 54 16	2005 Nov 18	3600	1.0/1.0	390/580
HE 0134–1519	01 37 05.4	−15 04 23	2005 Nov 17	3600	1.0/1.0	390/580
			2005 Nov 20	10800	0.8/0.8	346/760
HE 0233–0343	02 36 29.7	−03 30 06	2005 Nov 17	3600	0.8/0.8	390/580
			2005 Nov 18	7200	1.0/0.7	390/580
			2005 Nov 19	4940	0.8/0.7	346/760
			2005 Nov 20	3600	0.8/0.7	346/760
HE 0243–3044	02 45 16.4	−30 32 02	2005 Nov 18	5400	1.0/1.0	390/580
			2005 Nov 20	3600	0.8/0.7	437/760
HE 0411–3558[d,e]	04 13 09.0	−35 50 39	2005 Nov 17	3600	0.4/0.3	390/580
HE 0440–1049[e]	04 42 39.7	−10 43 24	2006 Apr 18	900	1.2/1.2	390/580
HE 0440–3426[e]	04 42 08.1	−34 21 13	2006 Apr 17	900	1.2/1.2	390/580
HE 0448–4806[e]	04 49 33.0	−48 01 08	2006 Apr 18	840	1.2/1.2	390/580
HE 0450–4902	04 51 43.3	−48 57 25	2006 Apr 17	3600	1.2/1.2	390/580
HE 0945–1435[f]	09 47 50.7	−14 49 07	2006 Apr 17	3600	1.2/1.2	390/580
			2006 Apr 18	7200	0.8/0.7	437/760
HE 1029–0546	10 31 48.2	−06 01 44	2006 Apr 17	3950	1.2/1.2	390/580
			2006 Apr 18	7200	0.8/0.7	390/580
HE 1218–1828	12 21 19.3	−18 45 34	2006 Apr 21	6000	1.2/1.2	390/580
			2006 Apr 21	3000	0.8/0.7	390/580
HE 1241–2907	12 44 13.0	−29 23 47	2006 Apr 17	3600	1.2/1.2	390/580
HE 1310–0536	13 13 31.2	−05 52 13	2006 Apr 17	3600	1.2/1.2	390/580
			2006 Apr 18	7200	0.8/0.7	437/760
HE 1429–0347[e]	14 32 26.1	−04 00 31	2006 Apr 17	1800	1.2/1.2	390/580
			2006 Apr 18	7200	0.8/0.7	437/760
HE 2159–0551[e]	22 02 16.4	−05 36 48	2006 Apr 18	900	0.8/0.7	390/580
HE 2208–1239[e]	22 10 53.3	−12 24 27	2006 Apr 18	600	0.8/0.7	390/580
HE 2238–4131	22 41 22.6	−41 15 57	2005 Nov 19	3600	1.2/1.2	390/580
HE 2239–5019	22 42 26.9	−50 04 01	2005 Nov 17	10800	1.0/0.8	390/580
HE 2331–7155	23 34 36.1	−71 38 51	2005 Nov 17	3600	0.8/0.8	390/580
			2005 Nov 20	7200	0.8/0.7	437/760

Notes.
[a] Blue slit/red slit.
[b] Spectrograph setting 390/580 = DIC1 (390+580), etc.
[c] CS 22942–019; CD-26:304.
[d] CS 22186–005.
[e] Frebel et al. (2006).
[f] Norris et al. (2013a).

excluded from the determination of the offset between the two temperature scales.

Surface gravity ($\log g$) estimates for the stars were determined from the Y^2 isochrones (Demarque et al. 2004), assuming an age of 10 Gyr (Yong et al. 2013) and an α-element enhancement of $[\alpha/\mathrm{Fe}] = +0.3$ (the isochrones exist with $[\alpha/\mathrm{Fe}] = 0.0$, $[\alpha/\mathrm{Fe}] = +0.3$, and $[\alpha/\mathrm{Fe}] = +0.6$). The isochrones extend in metallicity down to $[\mathrm{Fe/H}] = -3.5$, so for the six stars in the sample with metallicities in the range $-4.7 \leqslant [\mathrm{Fe/H}] \leqslant -3.5$, a linear extrapolation down to $[\mathrm{Fe/H}] = -4.7$ has been used to obtain the gravity estimate. The average difference between the listed surface gravities where the actual [Fe/H] have been used and the surface gravity obtained using the $[\mathrm{Fe/H}] = -3.5$ isochrone is small, on the order of 0.05 dex.

Figure 1 shows the $T_{\rm eff}$ versus $\log g$ diagram for the program stars with isochrones for three different metallicities: $[\mathrm{Fe/H}] = -1.9$, $[\mathrm{Fe/H}] = -2.5$, and $[\mathrm{Fe/H}] = -3.5$. All isochrones have $[\alpha/\mathrm{Fe}] = +0.3$ and an age of 10 Gyr. The sample shows a mixture of dwarfs, subgiants, and giants.

For five of the warmer stars in the sample, HE 0233–0343, HE 0411–3558, HE 0450–4209, HE 1241–2907, and HE 2239–5019, the isochrones returned two possible solutions for the gravity. For these five stars we have tried to derive spectroscopic gravities and/or checked the isochrone gravities by fitting profiles of gravity-sensitive lines. The gravity of stars can be determined spectroscopically by enforcing ionization equilibrium between lines formed by neutral atoms and lines formed by ions, e.g., Fe I and Fe II or Ti I and Ti II, taking advantage of the fact that Fe I and Ti I lines are not significantly gravity sensitive, while the Fe II and Ti II lines are. We performed this analysis for the stars where both Fe I and Fe II or Ti I and Ti II lines were detected. A check of the gravity can also be performed by fitting the profiles of gravity-sensitive lines. Lines such as Mg I and the Ca II H and K lines exhibit strong pressure-broadened wings in cool stars. We performed spectral syntheses of these lines using model atmospheres with

Table 2
Radial Velocities and Signal-to-noise Ratios

Stellar ID	V_r (km s^{-1})	$V_{r,\mathrm{err}}$ (km s^{-1})	S/N 3400 Å	S/N 4300 Å	S/N 6700 Å
HE 0010–3422	158.8	0.2	11	49	84
HE 0054–2542	−214.6	0.1	9	46	96
HE 0100–1622	28.6	0.3	3	17	39
HE 0109–4510	138.8	0.1	5	25	33
HE 0134–1519	244.0	1.0	14	54	75
HE 0233–0343	63.5	0.6	9	35	42
HE 0243–3044	39.8	0.3	9	14	32
HE 0411–3558	196.2	0.3	26	105	110
HE 0440–1049	158.9	3.0	16	65	86
HE 0440–3426	326.0	0.6	16	61	162
HE 0448–4806	133.5	0.7	10	44	68
HE 0450–4902	332.4	1.5	4	26	29
HE 0945–1435	144.8	0.4	12	44	80
HE 1029–0546	18.6	0.3	10	35	45
HE 1218–1828	147.1	0.5	4	19	33
HE 1241–2907	336.3	2.2	4	31	16
HE 1310–0536	113.2	1.7	1	39	65
HE 1429–0347	−143.3	0.4	3	71	129
HE 2159–0551	−131.3	0.8	2	50	72
HE 2208–1239	−43.1	0.6	5	55	102
HE 2238–4131	−42.0	0.3	2	13	32
HE 2239–5019	368.7	0.5	9	44	43
HE 2331–7155	210.6	0.8	6	51	120

the two possible gravities, keeping all other parameters constant, in order to see which of the two possible gravities yields the best fit in the wings of these lines. The result of these tests yielded subgiant gravities for HE 0233–0343, HE 0411–3558, and HE 2239–5019 and dwarf gravities for HE 0450–4209 and HE 1241–2907 (see Table 3).

The microturbulent velocity (ξ) was computed in the usual way, by forcing the abundances from individual Fe I lines to show no trend with reduced equivalent width, $\log(W_\lambda/\lambda)$. For HE 0233–0343, too few Fe I lines were present to determine the microturbulent velocity in this manner, so a fixed valued of $\xi = 2\,\mathrm{km\,s^{-1}}$ was used for this star, following Paper I.

Metallicities were determined from equivalent-width measurements of the Fe I lines. For a few stars we also detected a number of Fe II lines; for these stars there is good agreement between the abundance derived from the Fe II lines and that from the Fe I lines used for determining the temperature, gravity, and microturbulence.

The final stellar parameters and their estimated uncertainties are listed in Table 3.

2.2. Abundances

The elemental abundances were derived by synthesizing individual spectral lines and molecular bands. All abundances are derived under the assumption of 1D and local thermodynamic equilibrium and adopting the solar abundances from Asplund et al. (2009).

The 2011 version of MOOG (Sneden 1973; Sobeck et al. 2011) was used for the synthesis; this version of MOOG includes proper treatment of continuum scattering. For stars in the temperature range of our sample, the two main sources of opacity in stellar atmospheres are bound-free absorption from the negative hydrogen ion (H^-) and Rayleigh scattering from neutral atomic hydrogen. Their individual contributions to the total opacity depend on temperature and metallicity; at low temperature and low metallicity the contribution from Rayleigh scattering is almost equal to the contribution from bound-free absorption. Hence, when working with metal-poor stars it is especially important to model the scattering accurately to obtain the correct line intensities.

To perform the synthesis, we used the α-enhanced NEWODF grid of ATLAS9 atmosphere models (Castelli & Kurucz 2003), interpolated with software developed by C. Allende Prieto, to obtain the models matching the parameters of the stars (e.g., Reddy et al. 2003; Allende Prieto et al. 2004). The α-enhanced ATLAS9 models cover a range in T_{eff} from 3500 to 50,000 K, log g from 0.0 to 5.0 (cgs), for metallicities, [Fe/H], in the range −2.5 to +0.5 and [Fe/H] = −4.0. For the metallicity [Fe/H] = −3.5, models exists with temperatures in the range 3500–6500 K, and surface gravities ranging from 0.0 to 5.0.

We used atomic data from the *Gaia*/ESO line list version 4 (U. Heiter et al. 2015, in preparation) for the analysis. This list covers the lines in the range 4750–6850 Å and 8500–8950 Å. For lines not covered by the *Gaia*/ESO line list, atomic data from the VALD database (Kupka et al. 2000) were adopted. A number of the elements analyzed exhibit hyperfine splitting (Sc, Mn, Co, Y, Zr, La, Pr, Nd, and Eu). For those elements that only have lines in the region not covered by the *Gaia*/ESO line list, hyperfine splitting from Kurucz (1995) was used. The lines of Li, Ba, and Pb have both hyperfine splitting and isotopic shifts. The lines of Li and Ba are included in the *Gaia*/ESO line list, while Pb is not, so for this element data from Simons et al. (1989) were used.

Carbon and nitrogen abundances (or upper limits) and the isotopic ratios $^{12}C/^{13}C$ were obtained by synthesizing molecular bands, namely, the 4300 Å CH G band, the NH band at 3360 Å, and the CN bands at 3890 and 4215 Å. All molecular information is taken from Masseron et al. (2014) and T. Masseron (2015, private communication). Dissociation energies of 3.47, 3.42, and 7.74 eV were used for the species CH, NH, and CN, respectively.

When possible, N abundances were determined from synthesis of the CN bands using the C abundances computed from the CH band as fixed input. If no CN band was visible, the nitrogen abundance was derived from the NH band (which falls in a region of the spectra with substantially lower S/N). For stars where abundances could be derived from both bands the resultant N abundances, derived from the NH and CN bands, respectively, are compared in Figure 2. For low N abundances, the results from the two bands agree well, while a discrepancy is seen at high N, with higher abundances being derived from the NH band compared to the CN band. The reason for this discrepancy is not clear, but the physical parameters, such as line positions and *gf* values, are less well established for the NH band compared to the CN band, which could account, at least in part, for it.

The carbon abundance is coupled to the oxygen abundance through the CO molecule. Oxygen abundances or upper limits for the sample stars are derived from the 6300 Å line, but for the majority of our stars no reliable oxygen abundance could be obtained, so when deriving the carbon abundances we used a typical halo-star value of [O/Fe] = +0.4 for oxygen.

Molecular ^{13}CH features were identified for 11 of the stars in our sample. The $^{12}C/^{13}C$ isotopic ratios were determined from

Table 3
Stellar Photometry and Stellar Atmospheric Parameters

Star	V	$B-V$	R^a	$E(B-V)$	K^b	$(V-K)_o$	$T_{\rm eff}$ (±100 K)	log g (±0.3 dex)	[Fe/H] (±0.2 dex)	ξ (±0.3 km s^{-1})
HE 0010–3422[c]	15.48	0.095	1	0.017	12.34	⋯	5400	3.1	−2.7	2.4
HE 0054–2542	12.69	0.880	2	0.040	10.65	1.89	5300	2.7	−2.5	1.3
HE 0100–1622	15.82	0.837	1	0.021	13.85	1.87	5400	3.0	−2.9	1.1
HE 0109–4510	16.01	0.523	1	0.011	14.18	1.75	5600	3.3	−3.0	1.1
HE 0134–1519	14.47	0.463	1	0.016	12.68	1.71	5500	3.2	−4.0	1.5
HE 0233–0343	15.43	0.437	1	0.025	14.06	1.26	6100	3.4	−4.7	2.0
HE 0243–3044	16.13	0.833	1	0.019	14.17	1.83	5400	3.2	−2.6	0.9
HE 0411–3558	12.96	0.382	1	0.011	11.58	1.31	6300	3.7	−2.8	3.4
HE 0440–1049	⋯	⋯	⋯	0.107	⋯	⋯	5800	3.5	−3.0	1.6
HE 0440–3426	11.44	1.440	3	0.013	8.97	2.39	4800	1.6	−2.2	1.9
HE 0448–4806	12.35	1.100	3	0.021	11.21	1.04	5900	3.6	−2.3	1.2
HE 0450–4902	⋯	⋯	⋯	0.009	⋯	⋯	6300	4.5	−3.1	1.2
HE 0945–1435	⋯	⋯	⋯	0.054	⋯	⋯	6300	4.5	−3.9	1.6
HE 1029–0546	15.63	0.355	1	0.043	14.37	1.10	6650[d]	4.3	−3.3	1.6
HE 1218–1828	16.34	0.493	1	0.043	14.70	1.48	5900[d]	3.5	−3.4	1.8
HE 1241–2907	⋯	⋯	⋯	0.071	⋯	⋯	6900	3.8	−3.0	1.8
HE 1310–0536	14.35	0.708	1	0.043	11.90	2.29	5000	1.9	−4.2	2.2
HE 1429–0347	13.69	0.687	1	0.110	11.41	1.94	5000	1.9	−2.7	1.5
HE 2159–0551	⋯	⋯	⋯	0.060	9.85	⋯	4800	1.5	−2.8	2.1
HE 2208–1239	⋯	⋯	⋯	0.041	⋯	⋯	5100	2.3	−2.9	2.0
HE 2238–4131	16.10	⋯	⋯	0.013	13.85	2.17	5200	2.5	−2.8	1.0
HE 2239–5019	15.85	0.393	1	0.009	14.28	1.50	6100	3.5	−4.2	1.8
HE 2331–7155	11.73	⋯	⋯	0.032	⋯	⋯	4900	1.5	−3.7	2.2

Notes.
[a] Source of V and $B-V$ color; 1 = Beers et al. (2007), 2 = Rossi et al. (2005), 3 = Høg et al. (2000).
[b] 2MASS Catalog (Skrutskie et al. 2006).
[c] The V and $B-V$ photometry for this star reported by Beers et al. (2007) is almost certainly in error.
[d] Photometric temperature.

the analysis of ^{13}CH features in the wavelength range from 4210 to 4235 Å. Figure 3 shows the synthesis of the ^{13}CH line at 4230 Å in HE 2208–1239 for three different isotopic ratios.

The derived elemental abundances, along with propagated uncertainties arising from the effects of uncertainties of the stellar parameters, continuum placement, and line information, are listed in Table 4 for the "normal" metal-poor (hereafter NMP) stars, Table 5 for the CEMP-*no* stars, Table 6 for the CEMP-*s* stars, and Table 7 for the CEMP-*r* and CEMP-*r*/*s* stars. The ^{12}C/^{13}C isotopic ratios, where available, are listed in Table 8.

3. RESULTS

The abundance analysis yielded abundances or upper limits for 18 elements: Li, C, N, Na, Mg, Al, Si, Ca, Sc, Ti, Cr, Mn, Fe, Co, Ni, Sr, Ba, and Eu, for all the stars in the sample, plus abundances or upper limits of Y, Zr, La, Ce, Pr, Nd, Sm, Gd, Dy, Er, and Pb, for the CEMP-*s*, CEMP-*r*, and CEMP-*r*/*s* stars in the sample.

As many of our sample stars are carbon enhanced, resulting in blended lines, we have chosen to perform spectral synthesis to derive the abundances of individual elements, whereas abundances for the comparison sample of Yong et al. (2013) were derived mostly from equivalent-width measurements. All other aspects of the analysis are the same for the two samples; thus, by combining them, we have a sample of over 200 homogeneously analyzed metal-poor stars. As a demonstration, we have derived abundances for HE 0146–1548 from the sample of Yong et al. (2013). These are listed in Table 9 along with the abundances listed in Yong et al. (2013). As can be seen, the two sets of abundances derived for this star agree very well.

The combined sample includes examples of all the different stellar abundance patterns that are commonly found at very low metallicity, for both carbon-enhanced stars (all four subclasses are represented) and non-carbon-enhanced stars. With this variety, and the fact that the combined sample includes some of the most metal-poor stars known, we are able to carry out a more detailed investigation of the signatures of our Galaxy's early chemical evolution than previously possible.

Yong et al. (2013) did not present Ba and Eu abundances for all the stars in their sample. However, abundances of these two elements are essential for the classification of CEMP stars (CEMP-*no*: [Ba/Fe] < 0, CEMP-*s*: [Ba/Fe] > +1, [Ba/Eu] > +0.5, CEMP-*r*: [Eu/Fe] > +1, CEMP-*r*/*s*: 0.0 < [Ba/Eu] < +0.5); thus, we have searched the literature for Ba and Eu abundances for the full sample of CEMP stars from Yong et al. (2013). These additional abundances are listed in Table 10. The supplemental abundances are only used for classification of the CEMP stars and not included in the plots, as they have not been derived in the same homogeneous manner as the abundances presented here. Table 10 also includes upper limits for Ba in HE 0107–5240, HE 0557–4840, and HE 1327–2326, as these all lie in the sparsely populated region with [Fe/H] < −4.0; we include them in our plots. The combined sample includes 143 NMP, 32 CEMP-*no*, 30 CEMP-*s*, 4 CEMP-*r*, and 4 CEMP-*r*/*s* stars.

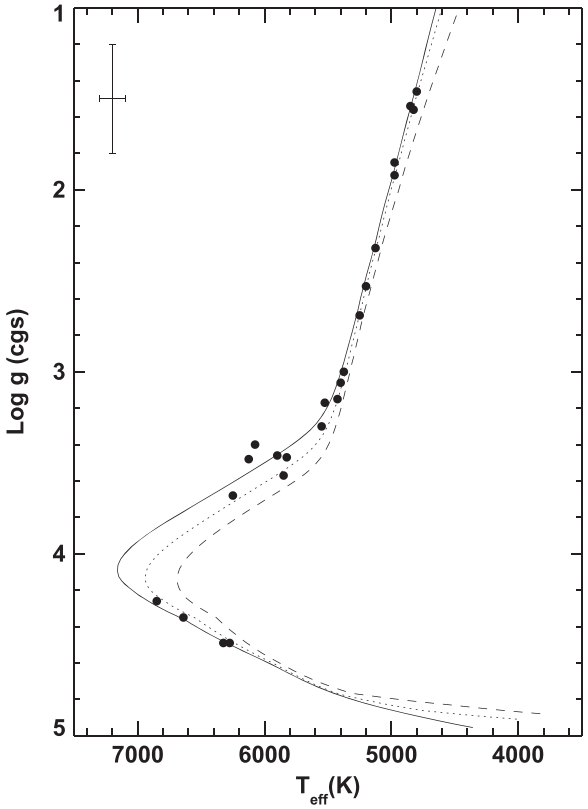

Figure 1. $T_{\rm eff}$ vs. log g diagram for the program stars, overplotted with 10 Gyr isochrones for three different metallicities: [Fe/H] = −3.5 (solid line), [Fe/H] = −2.5 (dotted line), and [Fe/H] = −1.9 (dashed line). All of the isochrones have [α/Fe] = +0.3. A representative error bar on the derived parameters is shown in the upper left.

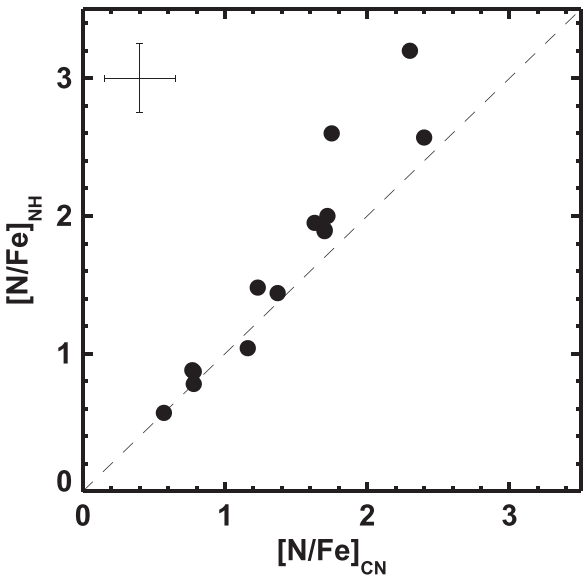

Figure 2. Comparison of nitrogen abundances estimated from the NH (3360 Å) and the CN (3890 Å) bands for stars where abundances could be derived from both bands. The dashed line is the one-to-one correlation. A representative error bar on the abundances ratios is shown in the upper left.

3.1. Carbon and Nitrogen

Carbon and nitrogen are among the first elements to be synthesized in the universe following the big bang. Yet our understanding of the abundances of these two elements found in the most metal-poor stars of our Galaxy is still limited. It is recognized that the observed carbon and nitrogen abundances of a given star are subject to change as the star evolves past the main sequence and up the red giant branch. Material that has been C-depleted and N-enhanced in the lower layers of a stellar atmosphere is transported to the surface of the star via mixing, enhancing N at the expense of C at the surface of the star. Thus, if we require the abundances of these two elements at the time when the star was born, in order to better constrain its progenitor, we need to correct the abundances of C and N for these evolutionary effects.

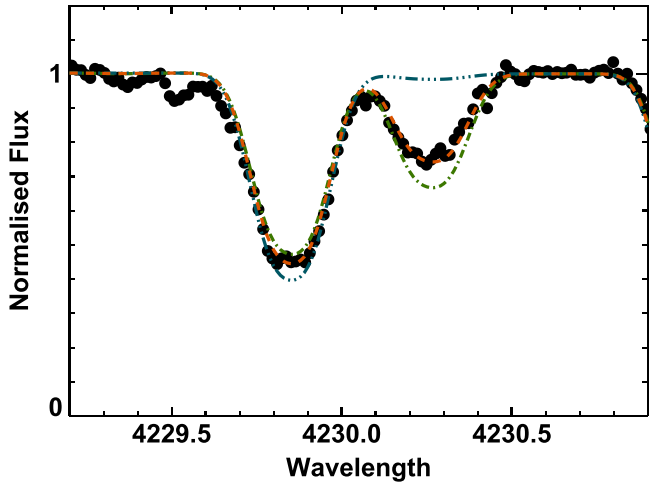

Figure 3. Synthesis of the ^{13}CH line at 4230 Å in HE 2208–1239 for three different isotopic ratios; 100% ^{12}CH (blue), ^{12}C/^{13}C = 79/21 (red), and ^{12}C/^{13}C = 70/30 (green).

Placco et al. (2014a) have developed a method for correcting the C abundances in metal-poor stars according to the evolutionary state of the star, based on the STARS stellar evolution code (Eggleton 1971; Stancliffe & Eldridge 2009) and thermohaline mixing as described in Stancliffe et al. (2009). We have corrected the C abundances for the giant stars in our sample using this method; for the Yong et al. (2013) sample we have used the corrections listed in Placco et al. (2014a), while corrections for our own sample can be seen in Table 11 (only including the nonzero corrections). For the remainder of this work we employ the corrected C abundances, unless stated otherwise. Note that no explicit correction is currently made for N.

3.1.1. [C/N] > 0 versus [C/N] < 0 Stars

Many of the carbon-enhanced stars are also found to be enhanced in nitrogen. However, the minority of VMP, EMP, and UMP stars have both elements detected, a deficiency that surely needs to be addressed in the near future. Only 79 of the 193 stars in the sample of Yong et al. (2013) have detections of both C and N. In our sample of 23 stars, we detect C and N simultaneously for as many as 14 stars, increasing the number of stars with C and N detections in the combined sample by about 20%. In the combined sample we have 104 stars with both C and N detections, plus a few with a detection of either C or N and an upper limit on the other. Roughly equal numbers of these are NMP and CEMP stars.

Figure 4 shows the C and N abundances and the [C/N] ratios of our combined sample of stars as a function of metallicity. We have divided the stars into two groups—circles indicate

Table 4
Derived Abundances for "Normal" Metal-poor (NMP) Stars

[X/Fe]	HE 0109–4510	HE 0411–3558	HE 0945–1435	HE 1218–1828	HE 1241–2907	HE 1429–0347	HE 2159–0551	HE 2239–5019
[Fe/H]	−2.96 (0.20)	−2.81 (0.20)	−3.87 (0.20)	−3.43 (0.20)	−3.00 (0.20)	−2.71 (0.20)	−2.81 (0.20)	−4.15 (0.20)
A(Li)	+1.46 (0.18)	<+1.44 ⋯	+1.88 (0.19)	+1.94 (0.17)	<+2.41 ⋯	+0.62 (0.16)	<+0.44 ⋯	<+1.70 ⋯
[C/Fe]	+0.43 (0.26)	<+0.70 ⋯	<+2.00 ⋯	<+1.27 ⋯	<+2.00 ⋯	+0.31 (0.23)	−0.24 (0.28)	<+1.70 ⋯
[N/Fe]	+0.57 (0.25)	<+1.30 ⋯	<+2.10 ⋯	<+1.70 ⋯	<+2.60 ⋯	+1.89 (0.25)	+0.88 (0.29)	<+2.70 ⋯
[O/Fe]	<+2.30 ⋯	<+2.30 ⋯	<+4.00 ⋯	<+3.30 ⋯	<+3.90 ⋯	+0.90 (0.15)	<+1.10 ⋯	<+4.00 ⋯
[Na/Fe]	−0.10 (0.19)	+0.02 (0.15)	<−0.30 ⋯	−0.33 (0.16)	+0.87 (0.18)	+1.00 (0.32)	+0.14 (0.30)	<−0.30 ⋯
[Mg/Fe]	+0.29 (0.19)	+0.24 (0.15)	+0.11 (0.14)	+0.32 (0.17)	+0.18 (0.19)	+0.28 (0.19)	+0.41 (0.24)	+0.45 (0.15)
[Al/Fe]	−0.91 (0.20)	−0.59 (0.20)	<−0.50 ⋯	−0.57 (0.22)	<−0.60 ⋯	+0.00 (0.17)	−0.82 (0.23)	−0.57 (0.21)
[Si/Fe]	+0.74 (0.20)	⋯ ⋯	+0.31 (0.16)	+0.06 (0.18)	+0.03 (0.20)	+0.66 (0.16)	+0.23 (0.22)	+0.06 (0.15)
[Ca/Fe]	+0.26 (0.18)	+0.22 (0.15)	+0.12 (0.18)	+0.60 (0.17)	+0.21 (0.19)	+0.49 (0.18)	+0.17 (0.23)	+0.23 (0.15)
[Sc/Fe]	+0.07 (0.22)	+0.38 (0.18)	<−0.10 ⋯	+0.12 (0.20)	+0.34 (0.22)	−0.08 (0.22)	−0.13 (0.27)	+0.32 (0.16)
[Ti/Fe]	+0.22 (0.23)	+0.59 (0.14)	−0.04 (0.18)	+0.25 (0.16)	+0.28 (0.18)	+0.30 (0.18)	+0.24 (0.23)	+0.37 (0.17)
[V/Fe]	<+0.80 ⋯	<+1.00 ⋯	<+1.80 ⋯	<+1.30⋯	<+1.60 ⋯	+0.21 (0.17)	+0.17 (0.23)	<+2.00 ⋯
[Cr/Fe]	−0.47 (0.18)	−0.05 (0.17)	−0.17 (0.16)	−0.28 (0.19)	+0.04 (0.21)	−0.36 (0.18)	−0.40 (0.24)	+0.00 (0.17)
[Mn/Fe]	−1.02 (0.20)	−0.62 (0.20)	<−0.20 ⋯	−0.65 (0.22)	<+0.00 ⋯	−0.70 (0.20)	−0.45 (0.25)	<−0.10 ⋯
[Co/Fe]	+0.47 (0.21)	+0.16 (0.19)	<+1.00 ⋯	+0.38 (0.21)	<+1.00 ⋯	−0.11 (0.19)	−0.06 (0.25)	<+1.00 ⋯
[Ni/Fe]	+0.68 (0.21)	+0.10 (0.17)	+0.17 (0.14)	−0.06 (0.19)	+0.16 (0.21)	+0.00 (0.27)	−0.03 (0.30)	+0.24 (0.17)
[Zn/Fe]	<+0.80 ⋯	<+0.60 ⋯	<+1.80 ⋯	<+1.50 ⋯	<+1.40 ⋯	+0.19 (0.15)	+0.36 (0.21)	<+2.00 ⋯
[Sr/Fe]	+1.00 (0.21)	−0.54 (0.19)	<−0.90 ⋯	−0.51 (0.20)	−0.77 (0.22)	+0.10 (0.16)	+0.16 (0.22)	<−0.60 ⋯
[Ba/Fe]	<−1.30 ⋯	−0.95 (0.14)	< 0.00 ⋯	<−0.52 ⋯	<−0.30 ⋯	−0.34 (0.17)	−1.58 (0.23)	<+0.00 ⋯
[Eu/Fe]	<+1.10 ⋯	<+1.50 ⋯	<+2.20 ⋯	<+2.00 ⋯	<+2.40 ⋯	+0.47 (0.20)	−0.20 (0.25)	<+2.50 ⋯

Table 5
Derived Abundances for CEMP-*no* Stars

	HE 0100–1622	HE 0134–1519	HE 0233–0343	HE 0440–1049	HE 1310–0536	HE 2331–7155
[Fe/H]	−2.93 (0.20)	−3.98 (0.20)	−4.68 (0.20)	−3.02 (0.20)	−4.15 (0.20)	−3.68 (0.20)
A(Li)	<+1.12 ⋯	+1.27 (0.19)	+1.77 (0.18)	+2.00 (0.14)	<+0.80 ⋯	<+0.37 ⋯
[C/Fe]	+2.75 (0.29)	+1.00 (0.26)	+3.48 (0.24)	+0.69 (0.25)	+2.36 (0.23)	+1.34(0.26)
[N/Fe]	+1.90 (0.28)	<+1.00 ⋯	<+2.80 ⋯	<+0.62 ⋯	+3.20 (0.37)	+2.57 (0.28)
[O/Fe]	<+2.30 ⋯	<+2.90 ⋯	<+4.00 ⋯	<+2.50 ⋯	<+2.80 ⋯	<+1.70 ⋯
[Na/Fe]	>+1.00 ⋯	−0.24 (0.15)	<+0.50 ⋯	−0.04 (0.13)	+0.19 (0.14)	+0.46(0.30)
[Mg/Fe]	+0.64 (0.23)	+0.25 (0.14)	+0.59 (0.15)	+0.79 (0.14)	+0.42 (0.16)	+1.20(0.23)
[Al/Fe]	+0.46 (0.24)	−0.38 (0.20)	<+0.03 ⋯	−0.57 (0.20)	−0.39 (0.21)	−0.38 (0.21)
[Si/Fe]	⋯ ⋯	+0.05 (0.16)	+0.37 (0.15)	+0.80 (0.15)	<+0.25 ⋯	⋯ ⋯
[Ca/Fe]	+0.49 (0.22)	+0.10 (0.13)	+0.34 (0.15)	+0.50 (0.14)	+0.00 (0.20)	+0.20 (0.22)
[Sc/Fe]	⋯ ⋯	+0.00 (0.18)	<+0.70 ⋯	−0.12 (0.18)	−0.07 (0.16)	+0.09 (0.25)
[Ti/Fe]	+0.71 (0.25)	+0.11 (0.21)	+0.18 (0.17)	+0.23 (0.14)	+0.35 (0.18)	+0.26 (0.22)
[V/Fe]	+0.67 (0.22)	<+1.20 ⋯	<+2.50 ⋯	<+0.80 ⋯	<+0.90 ⋯	+0.30 (0.21)
[Cr/Fe]	+0.08 (0.23)	−0.22 (0.18)	<+0.50 ⋯	−0.14 (0.17)	−0.49 (0.26)	−0.45 (0.22)
[Mn/Fe]	−0.18 (0.24)	−0.65 (0.19)	<+0.20 ⋯	−0.60 (0.22)	−0.79 (0.20)	−0.96 (0.24)
[Co/Fe]	+0.28 (0.25)	+0.20 (0.18)	<+1.60 ⋯	+0.30 (0.19)	+0.28 (0.16)	+0.30 (0.23)
[Ni/Fe]	+0.37 (0.24)	+0.19 (0.19)	<+0.90 ⋯	+0.18 (0.17)	−0.12 (0.20)	−0.04 (0.29)
[Zn/Fe]	<+0.90 ⋯	<+1.20 ⋯	<+2.60 ⋯	<+0.80 ⋯	<+1.30 ⋯	<+0.70 ⋯
[Sr/Fe]	+0.25 (0.25)	−0.30 (0.19)	+0.32 (0.19)	−0.30 (0.19)	−1.08 (0.14)	−0.85 (0.20)
[Ba/Fe]	<−1.80 ⋯	<−0.50 ⋯	<+0.80 ⋯	−1.27 (0.15)	−0.50 (0.15)	−0.90 (0.21)
[Eu/Fe]	<+0.80 ⋯	<+1.50 ⋯	<+3.00 ⋯	<+1.50 ⋯	<+1.20 ⋯	<+0.50 ⋯

stars where [C/N] > 0 ([C/Fe] > [N/Fe]), and triangles indicate stars where [C/N] < 0 ([C/Fe] < [N/Fe]). As we do not have the N abundance corrections corresponding to the C corrections mentioned above, this plot only includes dwarfs, subgiants, and early giants, for which the corrections in C and N will not alter the [C/N] > 0 or [C/N] < 0 status of the star. For the remainder of this paper we refer to this subsample as the "C/N stars."

Figure 5 shows the number of each type of metal-poor star with either [C/N] > 0 or [C/N] < 0. There are clearly more stars with [C/N] > 0 than with [C/N] < 0. For the NMP stars the numbers are roughly equal, while the CEMP-*no* and especially the CEMP-*s* stars are of the [C/N] > 0 variety. From inspection of the bottom panel of Figure 4, none of the CEMP-*no* stars with [C/N] < 0 are found with metallicities above [Fe/H] > −3.4; all CEMP-*no* stars with [C/N] < 0 are at the extremely low metallicity end.

Examination of the abundance ratios for the remaining elements for these stars using this division between C- and N-dominated stars, plotted in Figures 6–9, indicates that [Fe/H] = −3.4 also serves as a dividing line for the Na and Mg abundances in CEMP-*no* stars. Below this metallicity, stars with large overabundances of these two elements appear, in contrast to the behavior above this metallicity. Two of the CEMP-*no* stars with [C/N] < 0, HE 1327–2326 and HE

Table 6
Derived Abundances for CEMP-*s* Stars

	HE 0054–2542	HE 0440–3426	HE 0450–4902	HE 1029–0546	HE 2238–4131
[Fe/H]	−2.48 (0.20)	−2.19 (0.20)	−3.07 (0.20)	−3.28 (0.20)	−2.75 (0.20)
A(Li)	<+0.57 ⋯	<+0.26 ⋯	<+1.98 ⋯	<+2.00 ⋯	<+0.30 ⋯
[C/Fe]	+2.13 (0.29)	+1.51 (0.25)	+2.03 (0.23)	+2.64 (0.20)	+2.63 (0.32)
[N/Fe]	+0.87 (0.27)	+0.78 (0.26)	+2.00 (0.29)	+2.90 (0.27)	+1.04 (0.33)
[O/Fe]	<+1.20 ⋯	+0.69 (0.17)	<+3.50 ⋯	<+3.70 ⋯	<+1.70 ⋯
[Na/Fe]	>+1.20 ⋯	+0.67 (0.30)	+0.23 (0.22)	⋯ ⋯	>+1.60 ⋯
[Mg/Fe]	+0.78 (0.23)	+0.43 (0.21)	+0.53 (0.20)	−0.03 (0.17)	+0.87 (0.29)
[Al/Fe]	+0.10 (0.21)	⋯ ⋯	−0.78 (0.26)	<−0.42 ⋯	+0.12 (0.28)
[Si/Fe]	⋯ ⋯	⋯ ⋯	+0.00 (0.21)	−0.03 (0.18)	⋯⋯
[Ca/Fe]	+0.40 (0.22)	+0.23 (0.20)	+0.70 (0.23)	+0.16 (0.20)	+0.43 (0.28)
[Sc/Fe]	⋯ ⋯	⋯ ⋯	+0.12 (0.24)	+0.33 (0.21)	⋯⋯
[Ti/Fe]	+0.42 (0.22)	+0.26 (0.20)	+0.58 (0.22)	+0.45 (0.20)	+0.44(0.28)
[V/Fe]	+0.28 (0.27)	+0.03 (0.19)	<+1.30 ⋯	<+1.20 ⋯	⋯ ⋯
[Cr/Fe]	−0.03 (0.22)	−0.12 (0.20)	+0.03 (0.21)	−0.08 (0.18)	+0.00 (0.28)
[Mn/Fe]	−0.38 (0.24)	−0.63 (0.22)	−0.73 (0.26)	−0.14 (0.24)	−0.63 (0.30)
[Co/Fe]	−0.13 (0.25)	−0.54 (0.21)	<+0.60 ⋯	+0.90 (0.25)	−0.02 (0.29)
[Ni/Fe]	−0.10 (0.27)	+0.03 (0.28)	+0.00 (0.20)	+0.34 (0.17)	+0.00 (0.34)
[Zn/Fe]	<+0.08 ⋯	+0.06 (0.18)	<+1.40 ⋯	<+1.60 ⋯	<+0.70 ⋯
[Sr/Fe]	+1.65 (0.20)	+0.33 (0.18)	+0.64 (0.26)	+0.07 (0.24)	+1.75 (0.27)
[Y/Fe]	+1.99 (0.23)	+0.33 (0.19)	⋯ ⋯	<+1.05 ⋯	+2.13 (0.28)
[Zr/Fe]	+2.26 (0.22)	+0.64 (0.20)	⋯ ⋯	<+1.70 ⋯	+2.38 (0.29)
[Ba/Fe]	+1.52 (0.26)	+0.46 (0.19)	+1.21 (0.20)	+0.80 (0.17)	+1.80 (0.28)
[La/Fe]	+1.63 (0.24)	+1.18 (0.20)	⋯ ⋯	⋯ ⋯	+2.32 (0.28)
[Ce/Fe]	+1.50 (0.23)	+0.89 (0.18)	⋯ ⋯	<+2.70 ⋯	+2.35 (0.27)
[Pr/Fe]	+1.60 (0.23)	+1.07 (0.20)	⋯ ⋯	⋯ ⋯	+2.26 (0.27)
[Nd/Fe]	+0.36 (0.23)	+0.30 (0.17)	⋯ ⋯	<+2.46 ⋯	+1.05 (0.26)
[Sm/Fe]	+1.33 (0.21)	+1.01 (0.24)	⋯ ⋯	⋯ ⋯	+1.70 (0.31)
[Eu/Fe]	+0.78 (0.23)	<+0.62 ⋯	<+2.00 ⋯	<+2.50 ⋯	+1.10(0.29)
[Gd/Fe]	+1.10 (0.24)	⋯ ⋯	⋯ ⋯	⋯ ⋯	⋯ ⋯
[Dy/Fe]	+1.20 (0.24)	+0.74 (0.21)	⋯ ⋯	⋯ ⋯	+1.70 (0.29)
[Er/Fe]	⋯ ⋯	+1.14 (0.21)	⋯ ⋯	⋯ ⋯	>+2.00 ⋯
[Pb/Fe]	<+1.50 ⋯	+1.64 (0.23)	<+3.00 ⋯	+3.34 (0.23)	<+2.00 ⋯

2323–0256, show large enhancements in Na, Mg, and Sr, while the other two stars, HE 1150–0428 and HE 1310–0536, both have [Mg/Fe] ∼ 0.4 and subsolar [Sr/Fe].

For the remainder of the elements we see the well-known abundance patterns found at low metallicity in these plots—moderate overabundances of the α-elements and very low star-to-star scatter for both the α- and iron-peak elements, with a large scatter for the neutron-capture elements.

An additional subclass of metal-poor stars has been defined for stars with [N/Fe] > +0.5 and [C/N] < −0.5, the so-called nitrogen-enhanced metal-poor (NEMP) stars (Johnson et al. 2007). These stars are expected to be the result of mass transfer from an intermediate-mass asymptotic giant branch (AGB) star that has undergone hot bottom burning and thereby produced large amounts of nitrogen. Very few of these stars are known to exist, so here we consider the six stars in our sample with [C/N] < 0 to see whether they are possible NEMP stars. Two of the stars, HE 1310–0536 and HE 2331–7155, are CEMP-*no* stars, and two, HE 1429–0347 and HE 2159–0551, are NMP stars. None of these exhibit excesses of neutron-capture elements, as would be expected for the NEMP stars; thus, they can be excluded from this class. This leaves HE 0010–3422 (a CEMP-*r* star) and HE 2208–1239 (a CEMP-*r*/*s* star) as NEMP candidates. The binary status of these two stars is not known, but future radial-velocity monitoring should be able to clarify whether they are consistent with an NEMP classification.

3.1.2. The Carbon Plateau(s)

Spite et al. (2013) suggested the presence of two separate plateaus or "bands" in the distribution of C abundances, as a function of [Fe/H], for VMP and EMP stars. The C abundances for stars with metallicities [Fe/H] > −3 appeared to cluster around the solar carbon abundance[8] (A(C) ∼ 8.5), while those with [Fe/H] < −3 (including the lowest-metallicity stars known) cluster around a lower C abundance, A(C) ∼ 6.5. These authors proposed that the two bands could be associated with differing astrophysical production sites for the C in these stars—those in the higher band being the result of mass transfer of C from an AGB companion (i.e., extrinsic enrichment), and those in the lower band being the result of C that is intrinsic to the star (that is, the C was already present in the interstellar medium [ISM] from which the star was born). It is useful to note that Spite et al. (2013) only used dwarfs and turnoff stars in their study, stars where the C abundances are not expected to be altered owing to evolutionary effects. The recent paper by Bonifacio et al. (2015) confirms the existence of the two carbon bands for a larger sample, including the stars from Yong et al. (2013).

We consider this question again with our new sample. Figure 10 shows the absolute carbon abundances, A(C), for the stars in our new sample (circles) along with those of Yong et al. (2013) (plus signs), as a function of [Fe/H]. The top panel

[8] Here we employ the standard notation that $A(\mathrm{X}) = \log \epsilon\ (\mathrm{X}) + 12.0$.

Table 7
Derived Abundances for CEMP-*r* and CEMP-*r*/*s* Stars

	CEMP-*r*		CEMP-*r*/*s*	
	HE 0010–3422	HE 0448–4806	HE 0243–3044	HE 2208–1239
[Fe/H]	−2.78 (0.20)	−2.26 (0.20)	−2.58 (0.20)	−2.88 (0.20)
A(Li)	<+1.11 ···	<+1.49 ···	<+0.97 ···	< +0.77 ···
[C/Fe]	+1.92 (0.31)	+2.24 (0.29)	+2.43 (0.27)	+1.30 (0.29)
[N/Fe]	+2.60 (0.27)	+1.44 (0.29)	+1.48 (0.28)	+1.95 (0.25)
[O/Fe]	<+2.02 ···	<+1.90 ···	<+1.90 ···	<+1.40 ···
[Na/Fe]	+1.00 (0.28)	> +0.70 ···	> +1.00 ···	··· ···
[Mg/Fe]	+0.34 (0.23)	+0.44 (0.20)	+1.08 (0.23)	+0.59 (0.20)
[Al/Fe]	−0.54 (0.21)	−0.23 (0.24)	+0.04 (0.22)	−0.32 (0.18)
[Si/Fe]	··· ···	··· ···	··· ···	··· ···
[Ca/Fe]	+0.26 (0.22)	+0.35 (0.20)	+0.12 (0.22)	+0.45 (0.19)
[Sc/Fe]	+0.45 (0.24)	+0.25 (0.23)	··· ···	+0.25 (0.19)
[Ti/Fe]	+0.59 (0.22)	+0.50 (0.20)	+0.43 (0.23)	+0.70 (0.19)
[V/Fe]	+0.73 (0.27)	+0.38 (0.21)	+0.73 (0.22)	+0.54 (0.25)
[Cr/Fe]	−0.23 (0.25)	−0.03 (0.22)	−0.07 (0.23)	−0.20 (0.22)
[Mn/Fe]	−0.71 (0.24)	−0.37 (0.26)	−0.47 (0.25)	−0.83 (0.22)
[Co/Fe]	+0.15 (0.25)	+0.04 (0.25)	+0.03 (0.24)	+0.10 (0.22)
[Ni/Fe]	+0.01 (0.27)	+0.14 (0.22)	+0.26 (0.30)	−0.10 (0.24)
[Zn/Fe]	+0.57 (0.21)	+0.33 (0.24)	<+0.50 ···	+0.36 (0.18)
[Sr/Fe]	+0.85 (0.20)	+1.10 (0.23)	+0.97 (0.21)	+0.50 (0.17)
[Y/Fe]	+1.01 (0.23)	+0.93 (0.22)	+0.99 (0.22)	+0.37 (0.20)
[Zr/Fe]	+1.08 (0.22)	+1.10 (0.21)	+1.06 (0.23)	+0.84 (0.19)
[Ba/Fe]	+1.54 (0.26)	+1.78 (0.20)	+1.96 (0.22)	+1.68 (0.23)
[La/Fe]	+2.21 (0.24)	+2.33 (0.23)	+2.51 (0.23)	+1.96 (0.21)
[Ce/Fe]	+1.99 (0.23)	+2.20 (0.23)	+2.32 (0.21)	+1.80 (0.21)
[Pr/Fe]	+2.00 (0.20)	+2.24 (0.22)	+2.48 (0.22)	+1.77 (0.20)
[Nd/Fe]	+1.30 (0.23)	+1.46 (0.22)	+1.69 (0.20)	+1.06 (0.20)
[Sm/Fe]	+1.97 (0.21)	+2.09 (0.21)	+2.18 (0.26)	+1.76 (0.18)
[Eu/Fe]	+1.72 (0.23)	+1.87 (0.23)	+1.90 (0.24)	+1.52 (0.21)
[Gd/Fe]	··· ···	+1.92 (0.24)	+2.35 (0.23)	+1.61 (0.22)
[Dy/Fe]	··· ···	+1.89 (0.23)	+1.80 (0.24)	··· ···
[Er/Fe]	··· ···	+2.78 (0.22)	+2.64 (0.24)	+1.97 (0.20)
[Pb/Fe]	+2.62 (0.27)	+3.17 (0.29)	+3.07 (0.25)	+1.70 (0.36)

Table 8
$^{12}C/^{13}C$ Isotopic Ratios

Star	$^{12}C/^{13}C$	Type
HE 0010–3422	5	CEMP-*r*
HE 0054–2542	16	CEMP-*s*
HE 0100–1622	13	CEMP-*no*
HE 0134–1519	>4	CEMP-*no*
HE 0233–0343	>5	CEMP-*no*
HE 0243–3044	10	CEMP-*r*/*s*
HE 0440–3426	13	CEMP-*s*
HE 0448–4806	10	CEMP-*r*
HE 1029–0546	9	CEMP-*s*
HE 1310–0536	3	CEMP-*no*
HE 2208–1239	4	CEMP-*r*/*s*
HE 2238–4131	16	CEMP-*s*
HE 2331–7155	5	CEMP-*no*

Table 9
Abundances Derived for HE 0145–1548

[X/Fe]	Yong et al. (2013)	This Work
[C/Fe]	+0.84	+0.80
[Na/Fe]	+1.17	+1.15
[Mg/Fe]	+0.87	+0.86
[Al/Fe]	+0.14	+0.10
[Si/Fe]	+0.50	<+0.66
[Ca/Fe]	+0.22	+0.19
[Ti/Fe]	+0.17	+0.15
[Cr/Fe]	−0.38	−0.39
[Mn/Fe]	−0.59	−0.64
[Co/Fe]	+0.30	···
[Ni/Fe]	+0.05	+0.07
[Sr/Fe]	−0.38	−0.34
[Ba/Fe]	−0.71	−0.78

shows only the CEMP stars, while the bottom panel shows both the CEMP and NMP stars. There does indeed appear to exist a difference in the C abundances for the lower-metallicity and higher-metallicity CEMP stars, as suggested by Spite et al. (2013). Our larger data set exhibits a smoother transition between the two bands in the metallicity region [Fe/H] ∼ −3.4 to [Fe/H] ∼ −3.2. Bonifacio et al. (2015) identify four CEMP-*no* stars with C abundances on the high carbon band. In Figure 10 it can be seen that our sample includes three CEMP-*no* stars with C abundances on the high band. These three stars —HE 0100–1622 ([Ba/Fe] < −1.80), HE 2202–4831 ([Ba/Fe] = −1.28), and HE 2356–0410 ([Ba/Fe] = −0.80)—are all confirmed CEMP-*no* stars; hence, they challenge the interpretation of the two bands as being solely due to extrinsic and intrinsic processes. We note that the binary status of this

Table 10
Ba and Eu Abundances from the Literature

Star	[X/Fe]	References
	Ba	
BD −18°5550	−0.74	François et al. (2007)
CS 22880–074	+1.31	Aoki et al. (2002b)
CS 22892–052	+0.99	Sneden et al. (2003)
CS 22897–008	−1.00	François et al. (2007)
CS 29498–043	−0.45	Aoki et al. (2002a)
CS 29516–024	−0.90	François et al. (2007)
CS 30301–015	+1.45	Aoki et al. (2002b)
CS 31062–050	+2.30	Aoki et al. (2002b)
HD 196944	+1.10	Aoki et al. (2002b)
HE 0107–5240	<+0.82	Christlieb et al. (2004)
HE 0557–4840	<+0.03	Norris et al. (2007)
HE 1300+0157	<−0.63	Cohen et al. (2008)
HE 1327–2326	<+1.46	Aoki et al. (2006)
	Eu	
CS 22880–074	+0.50	Aoki et al. (2002b)
CS 22892–052	+1.64	Sneden et al. (2003)
CS 22948–027	+1.57	Aoki et al. (2002b)
CS 29497–034	+1.80	Barbuy et al. (2005)
CS 29503–010	+1.69	Allen et al. (2012)
CS 30301–015	+0.20	Aoki et al. (2002b)
CS 31062–012	+1.62	Aoki et al. (2002b)
CS 31062–050	+1.84	Aoki et al. (2002b)
HD 196944	+0.17	Aoki et al. (2002b)
HE 0143–0441	+1.46	Cohen et al. (2006)
HE 0336+0113	+1.18	Cohen et al. (2013)
HE 1031–0020	<+0.87	Cohen et al. (2006)
HE 2158–0348	+0.80	Cohen et al. (2006)

Table 11
Carbon Abundances Corrected for Stellar-evolution Effects

Star	log g	[Fe/H]	$[C/Fe]_{original}$	$[C/Fe]_{corrected}$	[N/Fe]
HE 0054–2542	2.69	−2.48	+2.13	+2.15	+0.87
HE 0440–3426	1.56	−2.19	+1.51	+1.64	+0.78
HE 1310–0536	1.85	−4.15	+2.36	+2.47	+3.20
HE 1429–0347	1.92	−2.71	+0.31	+0.45	+1.89
HE 2159–0551	1.46	−2.81	−0.24	+0.22	+0.88
HE 2208–1239	2.32	−2.88	+1.30	+1.31	+1.95
HE 2238–4131	2.53	−2.75	+2.63	+2.65	+1.04
HE 2331–7155	1.54	−3.68	+1.34	+1.69	+2.57

handful of stars is not currently known and would clearly be of great interest to constrain. If the CEMP-*no* stars found on the high carbon band are indeed the result of mass transfer in a binary system, it will be difficult to explain how large amounts of carbon but no or very small amounts of *s*-process elements have been transferred from their AGB companion.

We also see that CEMP-*r* and CEMP-*r*/*s* stars are found at both the high and low levels of C enhancement. It would be interesting to examine larger samples of these stars, in order to search for the possible dominance of either high or low carbon-abundance stars for either of these CEMP subclasses.

The large carbon enhancements found in the lowest-metallicity stars are expected to be related to the formation of low-mass stars in the early universe. It has been demonstrated that low-mass stars can form as a result of cooling of gas clouds

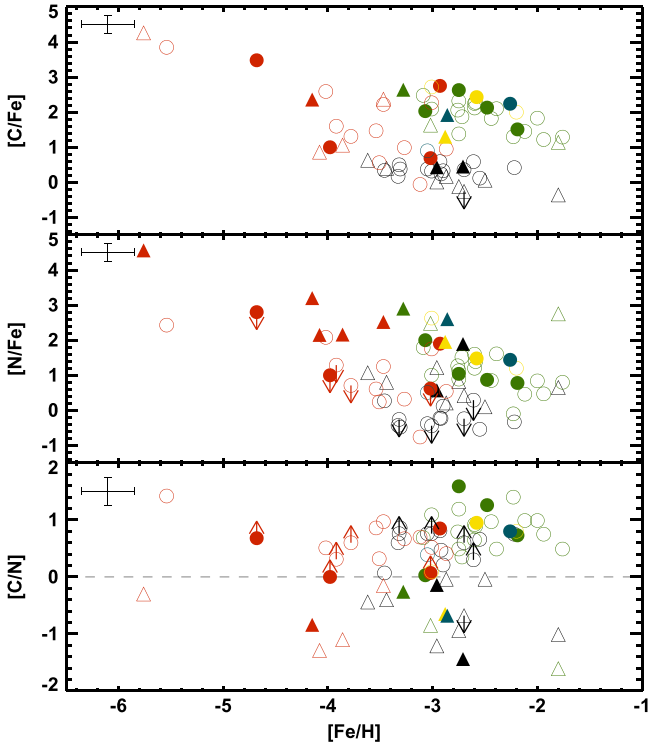

Figure 4. C and N abundances and [C/N] ratios for stars in this sample (filled symbols) and that of Yong et al. (2013) (open symbols). Circles represent stars with [C/N] > 0; triangles are stars with [C/N] < 0. Symbols are color-coded as follows: black—"normal" metal-poor (NMP) stars; red—CEMP-*no* stars; green—CEMP-*s* stars; blue—CEMP-*r* stars; yellow—CEMP-*r*/*s* stars. An approximate error bar for the sample stars is shown in the upper left of each panel.

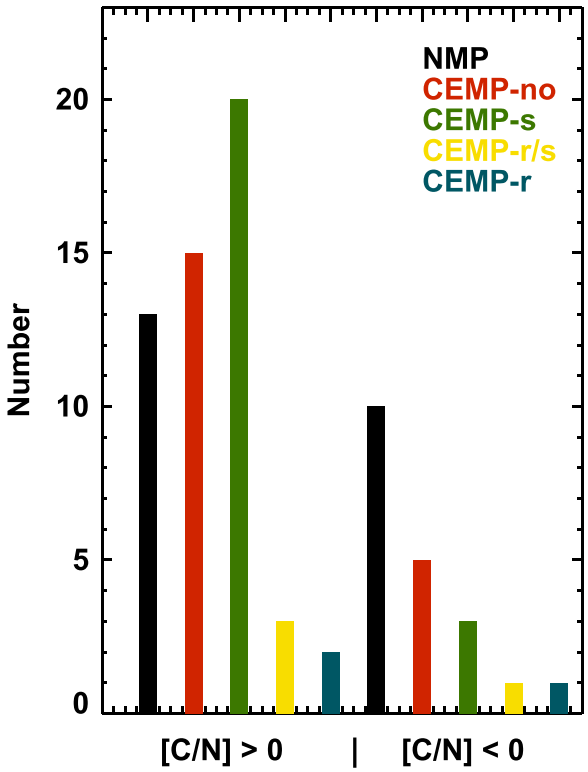

Figure 5. Number of stars with either [C/N] > 0 or [C/N] < 0 for the different types of metal-poor stars. Black: NMP stars; red: CEMP-*no* stars; green: CEMP-*s* stars; blue: CEMP-*r* stars; yellow: CEMP-*r*/*s* stars.

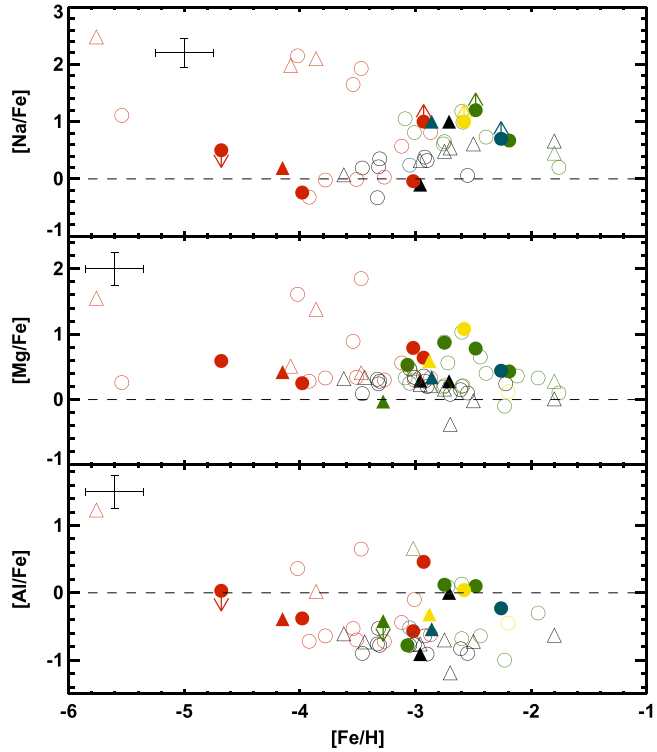

Figure 6. [Na/Fe], [Mg/Fe], and [Al/Fe] for the C/N stars. Color-coding of the stellar classes is as in Figure 4. An approximate error bar for the sample stars is shown in the upper left of each panel.

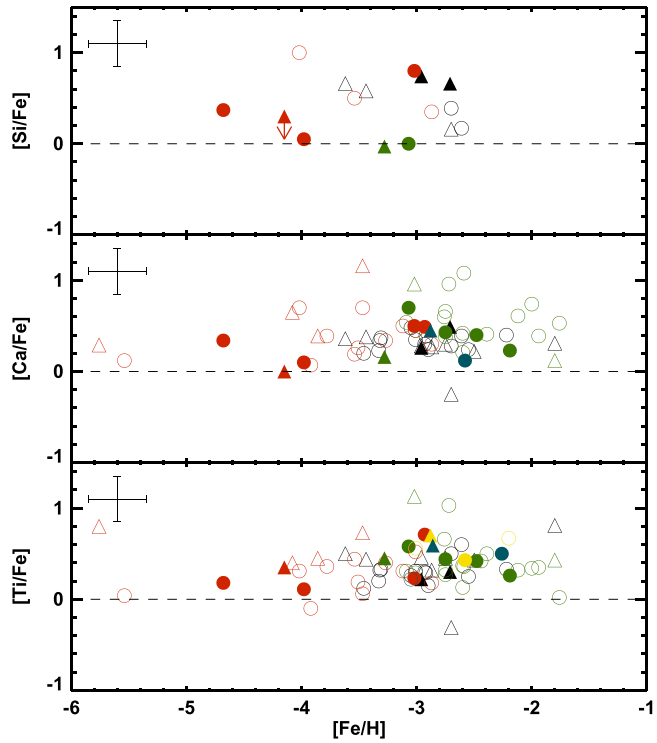

Figure 7. [Si/Fe], [Ca/Fe], and [Ti/Fe] for the C/N stars. Color-coding of the stellar classes is as in Figure 4. An approximate error bar for the sample stars is shown in the upper left of each panel.

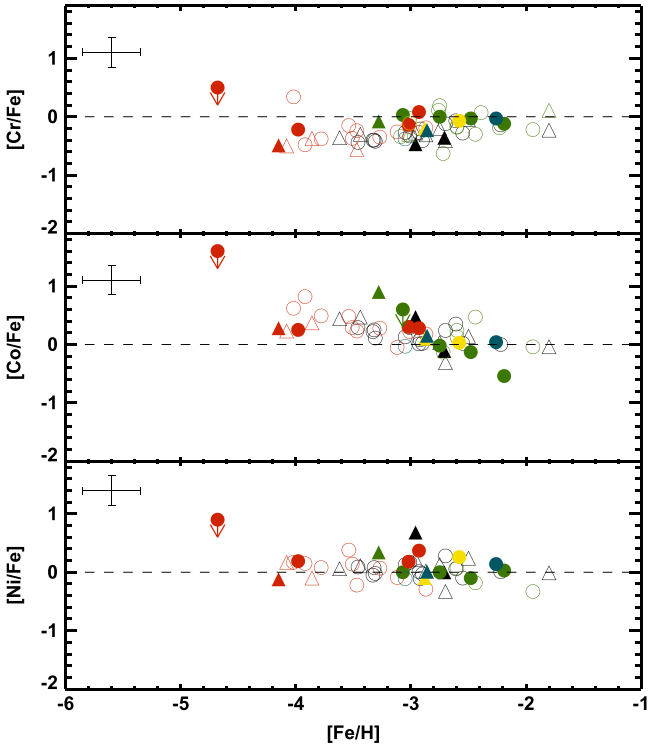

Figure 8. [Cr/Fe], [Co/Fe], and [Ni/Fe] for the C/N stars. Color-coding of the stellar classes is as in Figure 4. An approximate error bar for the sample stars is shown in the upper left of each panel.

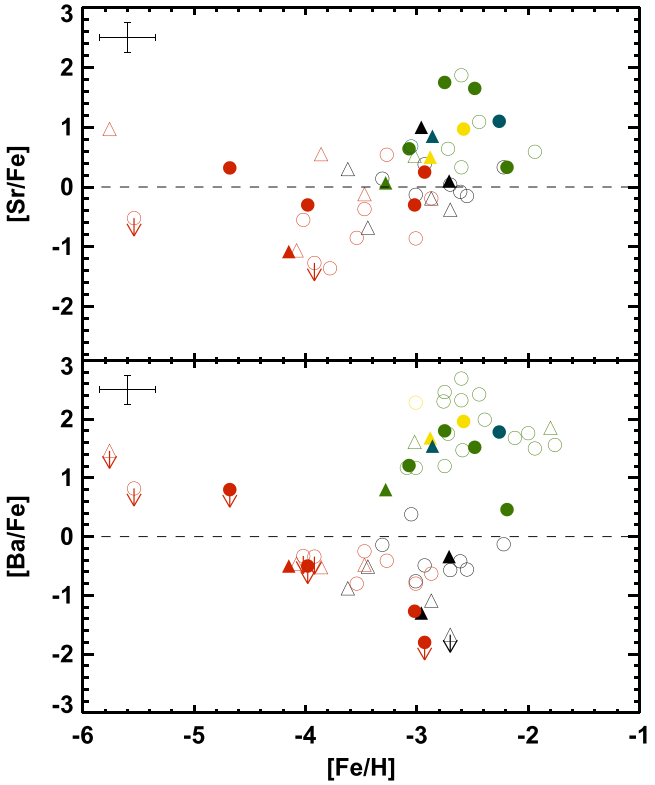

Figure 9. [Sr/Fe] and [Ba/Fe] for the C/N stars. Color-coding of the stellar classes is as in Figure 4. An approximate error bar for the sample stars is shown in the upper left of each panel.

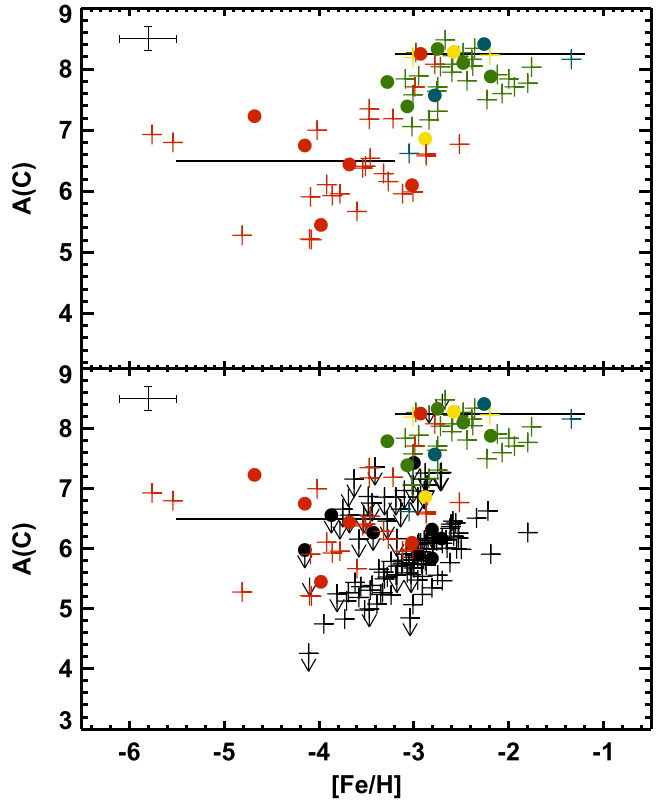

Figure 10. A(C) abundances for sample stars (circles) and stars from Yong et al. (2013) (plus signs). The top panel shows only CEMP stars, while all stars (including non-carbon-enhanced stars) are shown in the bottom panel. The two carbon bands are indicated by solid lines, and upper limits on individual C abundances are indicated by arrows. Symbols are color-coded as follows: black—"normal" metal-poor (NMP) stars; red—CEMP-*no* stars; green—CEMP-*s* stars; blue—CEMP-*r* stars; yellow—CEMP-*r*/*s* stars. An approximate error bar for the sample stars is shown in the upper left of each panel.

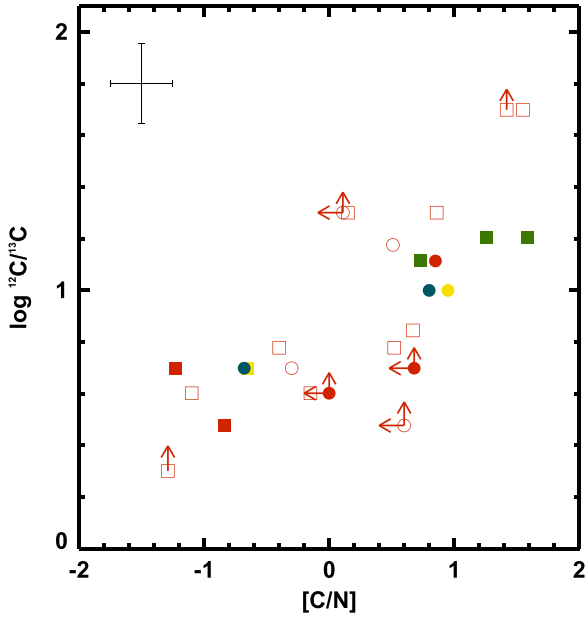

Figure 11. ^{12}C/^{13}C isotopic ratios, as a function of [C/N], for CEMP stars in the combined sample and from Norris et al. (2013b). The squares represent stars with log $g > 3.0$; circles represent stars with log $g < 3.0$. Filled symbols are from the combined sample; open symbols are from Norris et al. (2013b). The color-coding of the symbols is as in Figure 4. An approximate error bar for the sample stars is shown in the upper left of the panel.

via fine-structure lines of carbon and oxygen (Bromm & Loeb 2003; Frebel et al. 2007). Hence, the large C abundances found at the lowest metallicities in our sample support the formation of low-mass stars via this channel.

3.2. $^{12}C/^{13}C$ Isotopic Ratios

When internal mixing occurs in stars, whether that mixing is due to convection driven by rapid rotation ("spinstars"; see Meynet et al. 2006; Hirschi 2007; Maeder et al. 2014) or convection in AGB stars during their evolution (Herwig 2005), the carbon is transported from the core (spinstars) or from the surface (AGB stars) to the H-burning shell where the CNO cycle is active, the carbon is transformed into ^{13}C and ^{14}N. These signatures should be detectable in the ^{12}C/^{13}C isotopic ratio of a star. High ^{12}C/^{13}C and [C/N] ratios indicate only partial hydrogen burning by the CNO cycle, while low ^{12}C/^{13}C and [C/N] ratios are a signature of more complete burning by the CNO cycle (Maeder et al. 2014).

Chiappini et al. (2008) calculated the predicted ^{12}C/^{13}C isotopic ratio in the primordial ISM from which the first low-mass stars formed, if the first-generation stars were dominated by spinstars. They predict the ^{12}C/^{13}C isotopic ratio to be between 30 and 300, whereas if the first stars were not dominated by spinstars, the ratio would be ~4500 at [Fe/H] = −3.5 and as much as ~31,000 at [Fe/H] = −5.0. Models of mixing and fallback supernova (SN) events (Umeda & Nomoto 2003; Nomoto et al. 2013), suggested to occur in the early universe, also predict low ^{12}C/^{13}C isotopic ratios, as a result of the mixing in the pre-SN evolution stage between the He convective shell and H-rich envelope (Iwamoto et al. 2005). However, Maeder et al. (2014) predict differences in the ratio due to the different physical conditions and timescales for the production of ^{13}C during the stellar evolution of spinstars or in the SN explosion of the mixing and fallback models.

We have derived the ^{12}C/^{13}C isotopic ratios for 11 of our stars and lower limits for an additional two stars. Norris et al. (2013b) also investigated ^{12}C/^{13}C isotopic ratios in their sample of CEMP-*no* stars (which, except for BD +44°493 and Segue 1-7, all belong to the Yong et al. 2013 sample), but they were able to derive isotopic ratios for only 5 of their 15 stars; for the remaining they provided lower limits. Figure 11 plots the ^{12}C/^{13}C isotopic ratios, as a function of [C/N] (uncorrected C abundances), for the CEMP stars in our sample and those of Norris et al. (2013b). In this plot, circles represent stars with log $g < 3.0$ in which some internal CNO cycle processing might have changed the initial ^{12}C/^{13}C isotopic ratios, and squares represent stars with log $g > 3.0$ stars, which should have preserved their initial ^{12}C/^{13}C isotopic ratios.

We find low (~5) ^{12}C/^{13}C isotopic ratios for all of our CEMP-*no* stars, consistent with the equilibrium value for CNO-cycle processed material. This shows that the material from which these stars formed has undergone mixing, whether in spinstars or in some pre-SN evolution. The ^{12}C/^{13}C isotopic ratios found in the CEMP-*s* stars of our sample are generally higher (~13). This value is low enough to be a signature of H burning via the CNO cycle, which is also expected if the carbon excesses found in CEMP-*s* stars are transferred from an AGB companion, where multiple dredge-up events mix the material in the star. However, according to Bisterzo et al. (2012), current AGB models do not include sufficient mixing

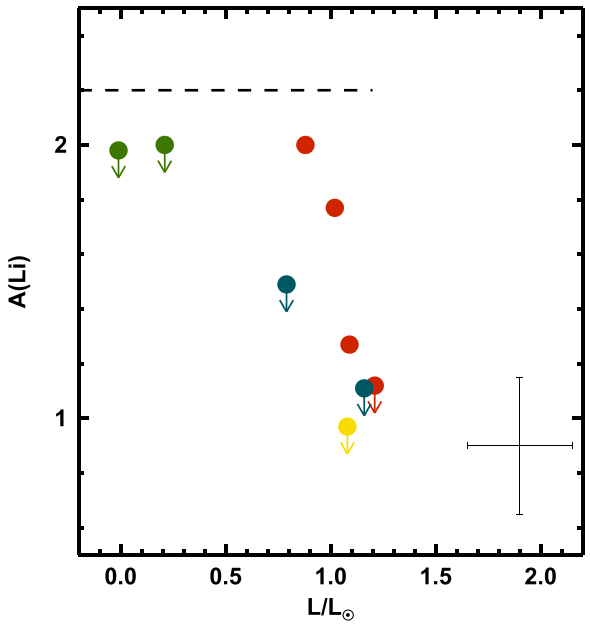

Figure 12. Absolute Li abundances, A(Li), and upper limits, indicated by arrows, as a function of luminosity, for the dwarf and subgiant CEMP stars in our sample. The Spite plateau lithium abundance (A(Li) = 2.2) is indicated with a dashed line. The color-coding of the symbols is as in Figure 4. An approximate error bar for the sample stars is shown in the lower right of the panel.

to replicate the low ^{12}C/^{13}C isotopic ratios found in CEMP-*s* stars.

3.3. Lithium

Paper I explored the lithium abundances detected in the UMP CEMP-*no* stars presented there, showing that all of these have Li abundances below the plateau found for non-carbon-enhanced metal-poor dwarfs at A(Li) = 2.05, the so-called Spite plateau (Spite & Spite 1982). This result supplements a similar finding by Masseron et al. (2012) and is consistent with the possible depletion of Li by the progenitors of CEMP-*no* stars suggested by Piau et al. (2006). In this model, the first, presumably massive, stars that formed in the universe are believed to have destroyed all of their Li. The observed Li abundances of the EMP and UMP stars are expected to be the result of the mixing of the Li-free material ejected from the first stars with the unprocessed ISM having an Li abundance generated by big bang nucleosynthesis. In this sense the lithium abundances of metal-poor main-sequence and subgiant stars can also be used to estimate the degree to which the material from the source star has been diluted.[9]

In this paper we present three additional CEMP-*no* stars, HE 0100–1622 with A(Li) < 1.12, HE 0440–1049 with A(Li) = 2.00, and HE 2331–7155 with A(Li) < 0.37. The last star is a giant with log g = 1.5, so this star has most likely internally depleted its initial lithium. The one star, HE 0440–1049, with a higher Li abundance, close to the Spite plateau value, also has the lowest carbon-abundance ratio among these stars ([C/Fe] = +0.69).

We have also examined the Li abundances for the CEMP-*s*, CEMP-*r*, and CEMP-*r*/*s* stars in our new sample, but only upper limits could be derived for these. Figure 12 shows the Li abundances and upper limits detected for all the dwarfs and subgiants in our sample, including those presented in Paper I, as a function of luminosity (Yong et al. 2013 did not present Li abundances for their stars). The additional CEMP-*no* stars follow the result from Paper I and Masseron et al. (2012) that all CEMP-*no* stars exhibit some level of Li depletion with respect to the Spite plateau.

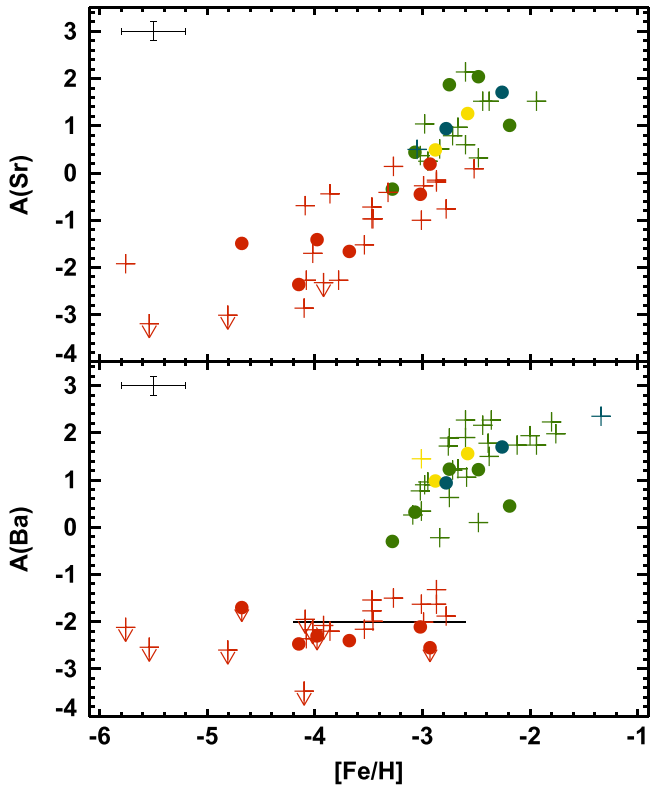

Figure 13. Absolute abundances of Sr and Ba, as a function of [Fe/H], for the CEMP stars. The suggested A(Ba) floor is indicated by the solid line. The symbols and color-coding are as in Figure 10. An approximate error bar for the sample stars is shown in the upper left of each panel.

3.4. Strontium and Barium

The strontium and barium abundances for VMP stars have received a great deal of attention over the past few years, in part because these two species are often the only neutron-capture elements for which abundances can be measured in the most metal-poor stars, making these two elements our only clue to the nature of neutron-capture processes at the earliest times in our Galaxy (Aoki et al. 2013b; Hansen et al. 2013; Roederer et al. 2014).

We have obtained detections or strong upper limits for Sr and Ba for all the stars in our sample, listed in Tables 4–7. Figures 13 and 14 shows the absolute Sr and Ba abundances as a function of [Fe/H]. Figure 13 shows only the CEMP stars, while Figure 14 shows all of the stars in our combined sample.

Inspection of Figures 13 and 14 indicates a clear grouping of the different classes of stars considered in our study. Recall that [Ba/Fe] is used to differentiate the CEMP-*no* stars from the

[9] We note that, although it is presented without attribution, the scenario proposed by Bonifacio et al. (2015) to account for the "meltdown" of the Spite Li plateau at low metallicities and the possible resolution of the so-called cosmological Li problem (their Section 5.2) is essentially the same as that proposed by Piau et al. (2006), as acknowledged by P. Bonifacio (2015, private communication to TCB).

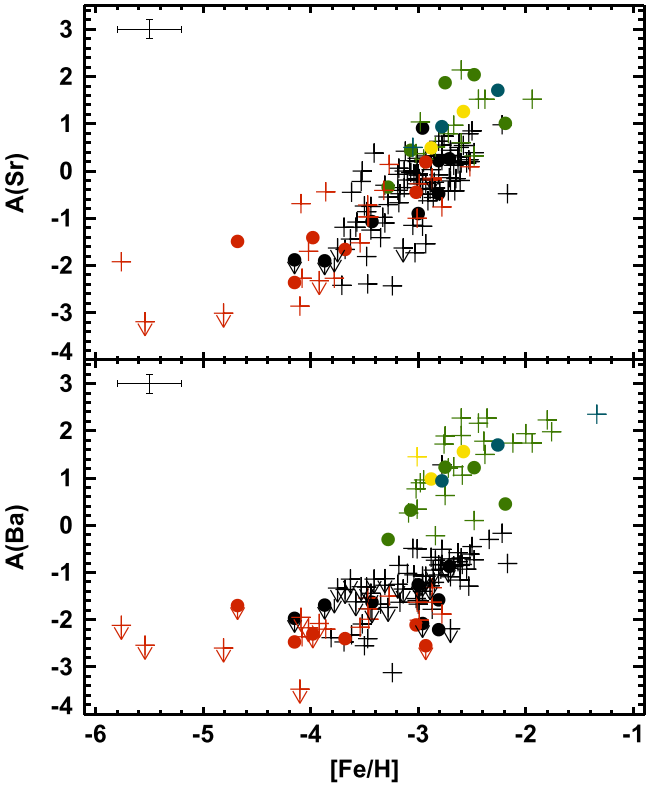

Figure 14. Absolute abundances of Sr and Ba, as a function of [Fe/H], for all of the stars in our combined sample. The symbols and color-coding are as in Figure 10. An approximate error bar for the sample stars is shown in the upper left of each panel.

CEMP-*s* and CEMP-*r*/*s* stars. The NMP (non-carbon-enhanced) stars exhibit a wide range of Ba abundances, from A(Ba) ∼ −4.0 to A(Ba) ∼ 0.0, while all the CEMP-*no* stars for which we have Ba detections exhibit Ba abundances of A(Ba) ∼ −2.0, independent of metallicity (most clearly seen when plotting only the CEMP stars; Figure 13). In contrast, the behavior of the Sr abundances for stars in our sample is substantially different. The individual classes of the stars in our sample are mixed together in a band showing decreasing A(Sr) with decreasing [Fe/H], but with a possible change in the trend at the lowest metallicity (around [Fe/H] ∼ −4.2). We emphasize that the area below [Fe/H] = −4 is only sparsely populated, with most stars only having an upper limit on Sr and Ba. The current data certainly suggest the presence of a floor in Ba at extremely low metallicity, but not for Sr; more detections of both species are strongly desired.

In the universe today, Ba is primarily produced by the main *s*-process in lower-mass AGB stars (Busso et al. 1999), but as this process was not operating in the early universe, the Ba found in the CEMP-*no* stars must have some alternative origin. It was shown by Frischknecht et al. (2010) that spinstars can produce some amount of slow neutron-capture elements such as Sr and Ba via the "weak" *s*-process, provided that some Fe seeds are available. It is possible that these elements can also be produced by the mixing and fallback models, by ejection of a tiny fraction of the heavy elements created in the explosion (Takahashi et al. 2014). Recently, Roederer et al. (2014) found four CEMP-*no* stars with clear *r*-process-element abundance patterns, confirming the early onset of the rapid neutron-capture process in the Galaxy. These authors also stress the need for Fe seeds for the weak *s*-process to operate efficiently in spinstars, meaning that it will not occur in a completely metal-free star.

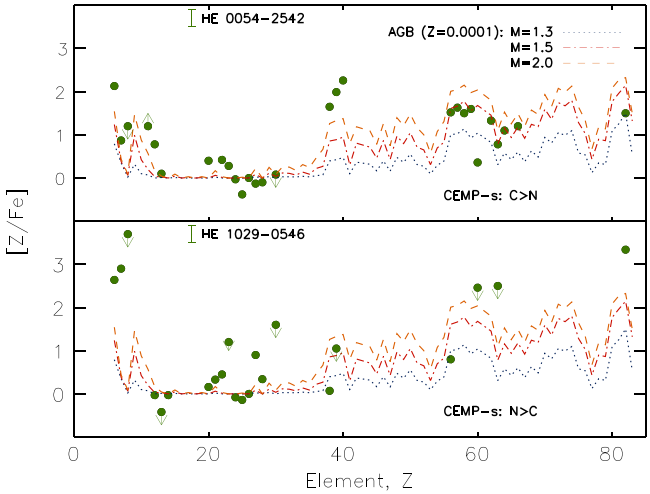

Figure 15. Observed elemental-abundance patterns for two CEMP-*s* stars, along with predicted yields for metal-poor AGB models of three different masses, 1.3, 1.5, and 2.0 $M_{\odot}$. A representative error bar on the derived abundances is shown next to the star name in each panel.

3.5. Abundance Profiles

The peculiar abundance patterns of the CEMP-*s* stars, showing large enhancements in carbon, nitrogen, and slow neutron-capture elements, are believed to be the result of mass transfer from an AGB companion in a binary system with the currently observed low-mass metal-poor star. Indeed, radial-velocity monitoring of CEMP-*s* stars is consistent with essentially all of these stars belonging to binary systems (Lucatello et al. 2005). Thus, the abundances observed in CEMP-*s* stars offer us a unique opportunity to constrain the properties of VMP AGB stars.

In the above division of stars into those with either [C/N] > 0 or [C/N] < 0, we see that the great majority of the CEMP-*s* stars have [C/N] > 0. To further investigate the properties of the AGB stars that created the elemental overabundances detected in CEMP-*s* stars, Figure 15 shows the observed elemental-abundance patterns of two CEMP-*s* stars—one having [C/N] > 0 and one with [C/N] < 0—along with the predicted yields from metal-poor (Z = 0.0001) AGB models of three different masses (1.3 $M_{\odot}$, 1.5 $M_{\odot}$, and 2.0 $M_{\odot}$), taken from the FRUITY database (Cristallo et al. 2009, 2011).

None of the models reproduce the large amounts of carbon and nitrogen detected in these stars, and none of the models have [C/N] < 0. The heavy neutron-capture elements for the CEMP-*s* star with [C/N] > 0 (HE 0054–2542) are well fit by the $M = 1.5\,M_{\odot}$ model, but none of the models produce sufficient amounts of the light neutron-capture elements (Sr, Y, and Zr) to match this star. The star with [C/N] < 0 (HE 1029–0546) is also not well fit by any of the models, but it does exhibit a general lower enhancement in *s*-process elements than the [C/N] > 0 star, pointing toward a lower-mass AGB star as the progenitor of HE 1029–0546.

Figure 16 shows the observed elemental-abundance patterns of the two CEMP-*r* and CEMP-*r*/*s* stars in our sample along with yields from the same metal-poor AGB stars. For the CEMP-*r* stars (left panels) none of the AGB models reproduce the observed C and N abundances, and while the most massive

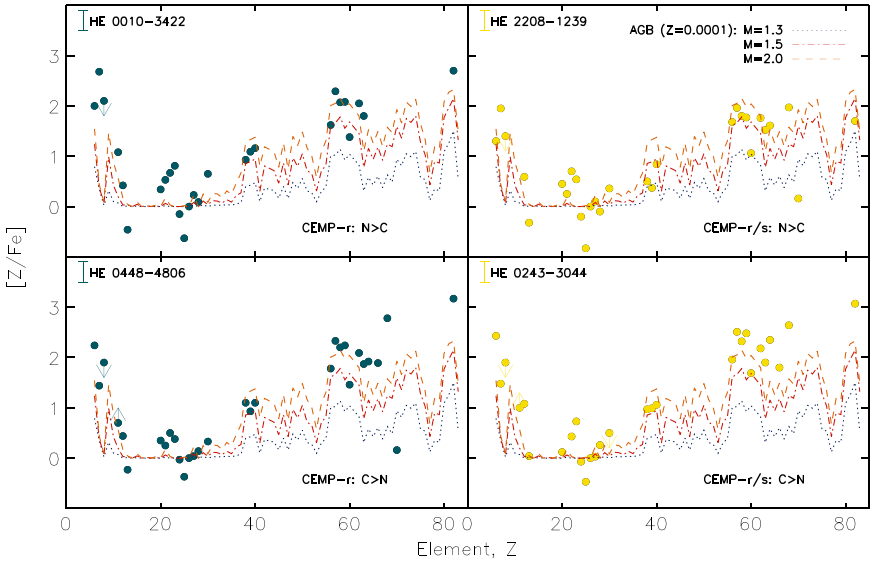

Figure 16. Observed elemental-abundance patterns for the two CEMP-*r* stars (left panels) and the two CEMP-*r/s* stars (right panels) in our sample, along with predicted yields for metal-poor AGB stars of three different masses, 1.3, 1.5, and 2.0 $M_{\odot}$. A representative error bar on the derived abundances is shown next to the star name in each panel.

AGB model does reproduce some of the observed abundances for the *n*-capture elements in HE 0010–3422, none of the models are a good fit for the abundances observed in HE 0448–4806. Considering the CEMP-*r/s* stars (right panels), the two most massive AGB models fit the observed C abundance for HE 2208–1239 and also some of the *n*-capture-element abundances observed in this star. For the other CEMP-*r/s* star, only the abundances for Sr, Y, and Zr can be reproduced by an AGB model.

It should also be noted that the material transferred from the AGB star and onto the currently observed CEMP star is expected to be mixed with the original stellar material via thermohaline mixing (Stancliffe et al. 2007; Stancliffe & Glebbeek 2008). The amount of dilution for the transferred material is not currently well constrained; hence, we have not included it in the comparison between observed abundances and AGB yields.

4. SUMMARY AND DISCUSSION

Below we summarize and discuss the abundance signatures found for the CEMP stars in our sample and what can be learned about the different progenitors that are currently suggested to account for the known subclasses of CEMP stars. However, one result that is consistently found in all abundance analyses of VMP stars, both carbon-enhanced and non-carbon-enhanced (see Cayrel et al. 2004; Yong et al. 2013), and which we confirm with our sample, is the small overabundance detected for the α-elements ($<$[Ca, Ti/Fe]$>\sim +0.35$) and the very low star-to-star scatter for both the α-elements ($\sim$0.15 dex) and the iron-peak elements ($\sim$0.20 dex).

4.1. CEMP-no Stars

The progenitors for the CEMP-*no* stars are thought to be either the massive fast-rotating stars (spinstars; Meynet et al. 2006; Hirschi 2007; Maeder et al. 2014), the proposed mixing and fallback SNe (Umeda & Nomoto 2003; Nomoto et al. 2013), or possibly contributions from both. Both models explain well the observed large overabundances of carbon and nitrogen. In the spinstar scenario, a star that exhibits [C/N] > 0 is the result of incomplete hydrogen burning via the CNO cycle, followed by mild mixing, whereas a star with [C/N] < 0 is the sign of more complete hydrogen burning (Maeder et al. 2014). Other abundance signatures detected in some CEMP-*no* stars, such as low $^{12}C/^{13}C$ isotopic ratios, which we find in all the CEMP-*no* stars where we could measure this ratio, and high Na, Mg and Al abundances, as detected in two of the CEMP-*no* stars with [C/N] < 0, can also be explained, according to Maeder et al. (2014), as the result of more mixing and processing of material in the spinstar.

Tominaga et al. (2014) have used "profile fitting" to show that the yields from mixing and fallback SNe also well fit the observed abundance patterns of CEMP-*no* stars. With a range of explosion energies and mass cuts, and by including mixing in some of the models, the authors fit the abundance profiles of 12 CEMP-*no* stars. Tominaga et al. (2014) also point out that the mixing and fallback SN model fits all the observed elements up to mass number $Z = 30$, including the α-elements and the iron-peak elements, while the spinstar models require a complementary SN contribution to create these elements in the appropiate proportion.

In our combined sample of 30 CEMP-*no* stars, we observe stars with both [C/N] > 0 and [C/N] < 0, but stars with [C/N] < 0 are only found at extremely low metallicity, [Fe/H] < −3.4, a metallicity below which the CEMP-*no* stars with large enhancements in Na, Mg, and Al also are found; above this metallicity the abundance spread is smaller. This indicates that the large degrees of internal mixing and processing required to produce the abundance pattern seen in stars such as HE 1327–2326 (Frebel et al. 2006) and HE 2323–0256 (Yong et al. 2013) were only operating at the very earliest times.

Our data also support the claim of Spite et al. (2013) and Bonifacio et al. (2015) for the presence of two carbon "bands" that comprise the distribution of the absolute carbon abundances for CEMP stars, although with a smoother transition between the bands than was found by these authors. The majority of the CEMP-*no* stars have carbon abundances falling on the lower band (A(C) $\sim$ 6.5), but a few with metalicities

above [Fe/H] > −3.0 have carbon abundances in the higher band (A(C) ∼ 8.5), indicating a different origin for the carbon found in these three stars as opposed to those with carbon abundances in the lower band.

We have inspected the ^{12}C/^{13}C isotope ratios for the CEMP stars in our sample and find low ^{12}C/^{13}C ratios for the CEMP-*no* stars we observed, again a signature of mixing in the progenitor stars. As noted above, both the spinstar models and the mixing and fallback models produce small ^{12}C/^{13}C ratios, but so far no values for expected ^{12}C/^{13}C ratios have been published for the SN models, making a comparison difficult.

Finally, we detect a "floor" in the absolute Ba abundances of CEMP-*no* stars, at an abundance level A(Ba) ∼ −2. This plateau only exists for the CEMP-*no* stars and must as such be a unique signature for the progenitors of these stars. As mentioned above, both the spinstar and the mixing and fallback models can produce some amount of neutron-capture elements. For the mixing and fallback models no yields have yet been published. In any case, the spinstars require Fe seeds; hence, some prior SN pollution is needed.

Roederer (2013) asked the question whether *any* stars, no matter at what low metallicity, completely lack neutron-capture elements. The CEMP-*no* stars are thought to be among the first low-mass stars to have formed, and although not all have detected neutron-capture elements, the discovery of a floor for the absolute Ba abundance of CEMP-*no* stars at extremely low metallicity supports the interpretation that some mechanism producing neutron-capture elements was present very early in the Galaxy.

Norris et al. (2013b) suggested that, in order to distinguish between spinstars and the mixing and fallback SNe for CEMP-*no* stars, one needs to investigate the abundances in these stars for elements that are produced in the deeper layers of the progenitor stars, such as Si and Ca. For our sample, the Ca abundances follow the general α-element trends of VMP halo stars, and only a few of our stars have detections for Si. More predicted elemental yields, over the full range of elements—both light and heavy— along with predicted ^{12}C/^{13}C ratios for both sets of progenitor models, and additional CEMP-*no* stars with measured Si abundances, are required to resolve this issue.

4.2. CEMP-*s* Stars

The origin of the CEMP-*s* stars has for some time been ascribed to mass transfer in a binary system from a now-extinct AGB star; however, there are still abundance signatures found in CEMP-*s* stars that the AGB models have difficulties in explaining.

For the 32 CEMP-*s* stars in our combined sample, we find that the great majority exhibit larger C enhancements than N enhancements, i.e., [C/N] > 0. However, we do find a few CEMP-*s* stars with [C/N] < 0, suggesting that a higher degree of H burning via the CNO cycle has occurred in the AGB companion in such cases. We also find higher ^{12}C/^{13}C isotopic ratios for the CEMP-*s* stars in this sample than found for the CEMP-*no* stars. However, the observed ratios are sufficiently low to require extensive mixing, which is also expected in an AGB star. Nevertheless, the observed ^{12}C/^{13}C ratios for CEMP-*s* stars are not reproduced by the AGB models (Bisterzo et al. 2012).

The CEMP-*s* stars in our sample have carbon abundances that place them on the higher of the two carbon bands of Spite et al. (2013), shown in Figure 10. Thus, there appears to be a maximum carbon abundance attained for the CEMP-*s* stars, which provides a constraint on the efficiency of the mass transfer and/or the production of C in AGB stars at very low metallicity.

4.3. CEMP-*r* and CEMP-*r*/*s* Stars

Small numbers of CEMP-*r*/*s* stars, and even fewer CEMP-*r* stars, are known, but we have identified two of each class in our sample. The first CEMP-*r* star to be found was CS 22892–052 (McWilliam et al. 1995; Sneden et al. 2003). This star is classified as both an *r*-II star[10] and a CEMP-*r* star and has an abundance pattern for the heavy *r*-process elements that well fits the scaled solar system *r*-process abundance pattern. It is not known with certainty what astrophysical site produces the carbon overabundances for CEMP-*r* stars, but radial-velocity monitoring of CS 22892–052 shows that this star is unlikely to be in a binary system (Hansen et al. 2011), suggesting that the carbon enhancements seen for CEMP-*r* stars are not the result of mass transfer in a binary system, but, more likely (as in the case of the CEMP-*no* stars), that they were born from an ISM that was previously polluted with carbon.

For CEMP-*r*/*s* stars, which exhibit contributions from both the *r*- and *s*-process, it has been proposed that they were born with their *r*-process-element abundances and then gain their carbon and *s*-process-element abundances via mass transfer in a binary system (Qian & Wasserburg 2003). Recently, it has also been suggested that these stars could be the result of the *i*-process, a process that is intermediate between the *r*- and the *s*-process, and thought to occur in high-mass "super-AGB" stars (Bertolli et al. 2013).

The general abundance patterns we detect in the two CEMP-*r* and two CEMP-*r*/*s* stars in our sample follow those of the other CEMP stars. However, we find both subclasses present on both the high and the low carbon-abundance bands shown in Figure 10. We also find ^{12}C/^{13}C isotopic ratios in these stars that match what is found both for the CEMP-*s* stars and for the CEMP-*no* stars. Larger samples of both CEMP-*r* and CEMP-*r*/*s* stars with available high-resolution, high-S/N spectra are clearly needed to obtain a more secure picture of the likely progenitor(s) of these objects. We have shown that one of the CEMP-*r* stars and one of the CEMP-*r*/*s* stars may be classified as NEMP stars; confirmation of their binary-pollution origin awaits future radial-velocity monitoring.

4.4. Outlook

We require still larger samples of the variety of low-metallicity stars presented in this paper to distinguish between the abundance patterns of stars representing the general trends and those that are just peculiar outliers. High-resolution spectroscopic follow-up of several large surveys, such as SkyMapper (Keller et al. 2007, 2014; Jacobson et al. 2015), TOPoS (Caffau et al. 2013), based on stars selected by SDSS/SEGUE (Yanny et al. 2009) (see also Aoki et al. 2013a), the CEMP-star searches from the HK survey, the HES, and the RAVE survey (Steinmetz et al. 2006) described by Placco et al. (2010, 2011, 2013, 2014a, and V. M. Placco et al. 2015, in preparation), and stars selected from LAMOST (Deng et al. 2012; Li et al. 2015), have increased in recent years and need to be expanded further. These surveys will soon provide

[10] [Eu/Fe] > +1.0 and [Ba/Eu] < 0.0 (Beers & Christlieb 2005).

more examples of CEMP-*r* and CEMP-*r*/*s* stars, for which our current samples are very limited. They will also enlarge the numbers of known CEMP-*s* and CEMP-*no* subclasses of carbon-enhanced stars. With detailed and homogeneous analyses of these stars, we can look forward to detecting the elemental abundance signatures that constrain the nature and sites of the nucleosynthesis events that first enriched the Milky Way.

This work was supported by Sonderforschungsbereich SFB 881 "The Milky Way System" (subproject A4) of the German Research Foundation (DFG). T.C.B. and V.P.M. acknowledge partial support for this work from grants PHY 08-22648, Physics Frontier Center/Joint Institute or Nuclear Astrophysics (JINA), and PHY 14-30152, Physics Frontier Center/JINA Center for the Evolution of the Elements (JINA-CEE), awarded by the U.S. National Science Foundation. C.J. H. was supported by a research grant (VKR023371) from VILLUM FONDATION and by Sonderforschungsbereich SFB 881 "The Milky Way System" (subproject A5) of the German Research Foundation (DFG). A.F. is supported by NSF CAREER grant AST-1255160. M.A., M.S.B., J.E.N., and D. Y. acknowledge support from the Australian Research Council (grants DP0342613, DP0663562, and FL110100012) for studies of the Galaxy's most metal-poor stars. Furthermore, we thank the referee for helpful comments.

Facilities: VLT:Kueyen, AAT, ATT, Blanco, CTIO:1.5 m, ESO:3.6 m, Mayall, SOAR,UKST

REFERENCES

Allen, D. M., Ryan, S. G., Rossi, S., Beers, T. C., & Tsangarides, S. A. 2012, A&A, 548, A34
Allende Prieto, C., Barklem, P. S., Lambert, D. L., & Cunha, K. 2004, A&A, 420, 183
Alonso, A., Arribas, S., & Martínez-Roger, C. 1996, A&A, 313, 873
Alonso, A., Arribas, S., & Martínez-Roger, C. 1999, A&AS, 140, 261
Aoki, W., Beers, T. C., Lee, Y. S., et al. 2013a, AJ, 145, 13
Aoki, W., Frebel, A., Christlieb, N., et al. 2006, ApJ, 639, 897
Aoki, W., Norris, J. E., Ryan, S. G., Beers, T. C., & Ando, H. 2002a, ApJL, 576, L141
Aoki, W., Ryan, S. G., Norris, J. E., et al. 2002b, ApJ, 580, 1149
Aoki, W., Suda, T., Boyd, R. N., Kajino, T., & Famiano, M. A. 2013b, ApJL, 766, L13
Asplund, M., Grevesse, N., Sauval, A. J., & Scott, P. 2009, ARA&A, 47, 481
Barbuy, B., Spite, M., & Spite, F. 2005, A&A, 429, 1031
Beers, T. C., & Christlieb, N. 2005, ARA&A, 43, 531
Beers, T. C., Flynn, C., Rossi, S., et al. 2007, ApJS, 168, 128
Beers, T. C., Preston, G. W., & Shectman, S. A. 1992, AJ, 103, 1987
Bertolli, M. G., Herwig, F., Pignatari, M., & Kawano, T. 2013, arXiv:1310.4578
Bessell, M. S. 2005, ARA&A, 43, 293
Bessell, M. S. 2007, PASP, 119, 605
Bisterzo, S., Gallino, R., Straniero, O., Cristallo, S., & Käppeler, F. 2012, MNRAS, 422, 849
Bonifacio, P., Caffau, E., Spite, M., et al. 2015, arXiv:1504.05963
Bonifacio, P., Monai, S., & Beers, T. C. 2000, AJ, 120, 2065
Bromm, V., & Loeb, A. 2003, Natur, 425, 812
Busso, M., Gallino, R., & Wasserburg, G. J. 1999, ARA&A, 37, 239
Caffau, E., Bonifacio, P., Sbordone, L., et al. 2013, A&A, 560, A71
Castelli, F., & Kurucz, R. L. 2003, IAU Symp. 210, Modelling of Stellar Atmospheres, ed. N. Piskunov, W. W. Weiss & D. F. Gray (San Francisco, CA: ASP), 20
Cayrel, R., Depagne, E., Spite, M., et al. 2004, A&A, 416, 1117
Chiappini, C., Ekström, S., Meynet, G., et al. 2008, A&A, 479, L9
Christlieb, N., Gustafsson, B., Korn, A. J., et al. 2004, ApJ, 603, 708
Christlieb, N., Schörck, T., Frebel, A., et al. 2008, A&A, 484, 721
Cohen, J. G., Christlieb, N., McWilliam, A., et al. 2008, ApJ, 672, 320
Cohen, J. G., Christlieb, N., Thompson, I., et al. 2013, ApJ, 778, 56
Cohen, J. G., McWilliam, A., & Shectman, S. 2006, AJ, 132, 137
Cristallo, S., Piersanti, L., Starniero, O., et al. 2011, ApJS, 197, 17
Cristallo, S., Starniero, O., Gallino, R., et al. 2009, ApJ, 696, 797
Dekker, H., D'Odorico, S., Kaufer, A., Delabra, B., & Kotzlowski, H. 2000, Optical and IR Telescope Instrumentation and Detectors, 4008, 534
Demarque, P., Woo, J. H., Kim, Y. C., & Yi, S. K. 2004, ApJS, 155, 667
Deng, L., Newberg, H. J., Liu, C., et al. 2012, RAA, 12, 735
Dopita, M., Hart, J., McGregor, P., et al. 2007, Ap&SS, 310, 255
Eggleton, P. P. 1971, MNRAS, 151, 351
François, P., Depagne, E., Hill, V., et al. 2007, A&A, 476, 935
Frebel, A., Christlieb, N., Norris, J. E., et al. 2006, ApJ, 652, 1585
Frebel, A., Johnson, J. L., & Bromm, V. 2007, MNRAS, 380, L40
Frebel, A., & Norris, J. N. 2015, arXiv:1501.06921
Frischknecht, U., Hirschi, R., Meynet, G., et al. 2010, A&A, 522, A39
Gustafsson, B., Edvardsson, B., Eriksson, N., et al. 2008, A&A, 486, 951
Hansen, C. J., Bergemann, M., Cescutti, G., et al. 2013, A&A, 551, A57
Hansen, T., Andersen, J., Nordström, B., Buchhave, L. A., & Beers, T. C. 2011, ApJL, 743, L1
Hansen, T., Hansen, C. J., Christlieb, N., et al. 2014, ApJ, 787, 162
Herwig, F. 2005, ARA&A, 43, 435
Hirschi, R. 2007, A&A, 461, 571
Høg, E., Frabricius, C., Makarov, V. V., et al. 2000, A&A, 355, L27
Iwamoto, N., Umeda, H., Tominaga, N., Nomoto, K., & Maeda, K. 2005, Sci, 309, 451
Jacobson, H., Keller, S., Frebel, A., et al. 2015, ApJ, in press
Johnson, J. A., Herwig, F., Beers, T. C., & Christlieb, N. 2007, ApJ, 658, 1203
Keller, S. C., Bessel, M. S., Frebel, A., et al. 2014, Natur, 506, 463
Keller, S. C., Schmidt, B. P., Bessel, M. S., et al. 2007, PASA, 24, 1
Kupka, F. G., Ryabchikova, T. A., Piskunov, N. E., Stempels, H. C., & Weiss, W. W. 2000, BaltA, 9, 590
Kurucz, R. L. 1995, in ASP Conf. Ser. 78, Astrophysical Applications of Powerful New Databases, ed. S. J. Adelman & W. L. Weise (San Francisco, CA: ASP), 78
Li, H., Zhao, G., Christlieb, N., et al. 2015, ApJ, 798, 110
Lucatello, S., Tsangarides, S., Beers, T. C., et al. 2005, ApJ, 625, 825
Maeder, A., Meynet, G., & Chiappini, C. 2014, arXiv:1412.5754
Masseron, T., Johnson, J. A., Lucatello, S., et al. 2012, ApJ, 751, 14
Masseron, T., Plez, B., van Eck, S., et al. 2014, A&A, 571, A47
McWilliam, A., Preston, G. W., Sneden, C., & Searle, L. 1995, AJ, 109, 2757
Meynet, G., Ekström, S., & Maeder, A. 2006, A&A, 447, 623
Nomoto, K., Kobayashi, C., & Tominaga, N. 2013, ARA&A, 51, 457
Norris, J. E., Bessell, M. S., Yong, D., et al. 2013a, ApJ, 762, 25
Norris, J. E., Christlieb, N., Korn, A. J., et al. 2007, ApJ, 670, 774
Norris, J. E., Ryan, S. G., & Beers, T. C. 1996, ApJS, 107, 391
Norris, J. E., Yong, D., Bessell, M. S., et al. 2013b, ApJ, 762, 28
Piau, L., Beers, T. C., Balsara, D. S., et al. 2006, ApJ, 653, 300
Placco, V. M., Frebel, A., Beers, T. C., & Stancliffe, R. J. 2014a, ApJ, 797, 21
Placco, V. M., Frebel, A., Beers, T. C., et al. 2013, ApJ, 770, 104
Placco, V. M., Frebel, A., Beers, T. C., et al. 2014b, ApJ, 781, 40
Placco, V. M., Kennedy, C. R., Beers, T. C., et al. 2011, AJ, 142, 188
Placco, V. M., Kennedy, C. R., Rossi, S., et al. 2010, AJ, 139, 1051
Preston, G. W., & Sneden, C. 2001, AJ, 122, 1545
Qian, Y. Z., & Wasserburg, G. J. 2003, ApJ, 588, 1099
Reddy, B. E., Tomkin, J., Lambert, D. L., & Allende Prieto, C. 2003, MNRAS, 340, 304
Roederer, I. U. 2013, AJ, 145, 26
Roederer, I. U., Preston, G. W., Thompson, I. B., Shectman, S. A., & Sneden, C. 2014, ApJ, 784, 158
Rossi, S., Beers, T. C., Sneden, C., et al. 2005, AJ, 130, 2804
Schlegel, D. J., Finkbeiner, D. P., & Davis, M. 1998, ApJ, 500, 525
Simons, J. W., Palmer, B. A., Hof, D. E., & Oldenborg, R. C. 1989, JOSAB, 6, 1097
Skrutskie, M. F., Cutri, R. M., Stiening, R., et al. 2006, AJ, 131, 1163
Sneden, C. 1973, ApJ, 184, 839
Sneden, C., Cowan, J. J., Lawler, J. E., et al. 2003, ApJ, 591, 936
Sobeck, J. S., Kraft, R. P., Sneden, C., et al. 2011, AJ, 141, 175
Spite, F., & Spite, M. 1982, A&A, 115, 357
Spite, M., Caffau, E., Bonifacio, P., et al. 2013, A&A, 552, A107
Stancliffe, R. J., Church, R. P., Angelou, G. C., & Lattanzio, J. C. 2009, MNRAS, 396, 2313
Stancliffe, R. J., & Eldridge, J. J. 2009, MNRAS, 396, 1699
Stancliffe, R., & Glebbeek, E. 2008, MNRAS, 389, 1828
Stancliffe, R., Glebbeek, E., Izzard, R. G., & Pols, O. R. 2007, A&A, 464, L57
Steinmetz, M., Zwitter, T., Siebert, A., et al. 2006, AJ, 132, 1645
Takahashi, K., Umeda, H., & Yoshida, T. 2014, ApJ, 794, 40
Tominaga, N., Iwamoto, N., & Nomoto, K. 2014, ApJ, 785, 98
Umeda, H., & Nomoto, K. 2003, Natur, 422, 871
Yanny, B., Newberg, H.-J., Johnson, J. A., et al. 2009, AJ, 137, 4377
Yong, D., Norris, J. E., Bessell, M. S., et al. 2013, ApJ, 762, 26